


## Small and Complex II: Characterizing the Disk and Stellar Envelope of Edge-on $z \sim 0$ Massive Compact Galaxies

A. SCHNORR-MÜLLER <sup>1</sup>, K. SLODKOWSKI CLERICI,<sup>1</sup> F. PINNA,<sup>2,3</sup> R. MERIB-DIAS,<sup>1</sup> M. TREVISAN,<sup>1</sup> T. V. RICCI,<sup>4</sup> F. FERRARI,<sup>5</sup> A. C. SANTIAGO-MENEZES,<sup>1,6</sup> W. L. BECKER,<sup>1</sup> AND F. PALACIOS<sup>1</sup>

<sup>1</sup>Universidade Federal do Rio Grande do Sul – Departamento de Astronomia – 91501-970, Porto Alegre-RS, Brazil

<sup>2</sup>Instituto de Astrofísica de Canarias, calle Vía Láctea s/n, E-38205 La Laguna, Tenerife, Spain

<sup>3</sup>Departamento de Astrofísica, Universidad de La Laguna, Avenida Astrofísico Francisco Sánchez s/n, E-38206 La Laguna, Spain

<sup>4</sup>Universidade Federal da Fronteira Sul – Campus Cerro Largo – 97900-000, Cerro Largo-RS, Brazil

<sup>5</sup>Universidade Federal do Rio Grande - Instituto de Matemática, Estatística e Física - 96203-900, Rio Grande-RS, Brazil

<sup>6</sup>European Southern Observatory, Alonso de Córdova 3107, Vitacura, Región Metropolitana, Chile

### ABSTRACT

We present multi-component photometric decompositions of  $r$ -band Hyper Suprime-Cam images for a sample of 75 edge-on massive compact galaxies (MCGs) at  $z < 0.1$ , selected as  $+2\sigma$  outliers in the stellar mass–velocity dispersion relation and  $-2\sigma$  outliers in the velocity dispersion–size relation. MCGs are composed of compact bulges and disks embedded within stellar envelopes of unclear physical nature. Comparing MCGs to a mass- and redshift-matched control sample of non-compact edge-on S0 galaxies with a similar three-component structure, we find that the smaller sizes of MCGs are not driven by a single component. MCGs host more compact bulges and envelopes ( $R_{e,\text{bulge}} \sim 0.3$  versus 0.5 kpc;  $R_{e,\text{env}} \sim 4.4$  versus 5.7 kpc), as well as shorter and thicker disks ( $h_R \sim 1.1$  versus 1.7 kpc;  $h_R/z_0 \sim 3.9$  versus 5.3). The sizes of the structural components are coupled, suggesting their formation processes are linked. Median bulge- and disk-to-total flux fractions are similar in both samples, with  $B/T \sim 0.3$  and  $D/T \sim 0.4$ . Envelope ellipticities span  $\epsilon_{\text{env}} \sim 0\text{--}0.7$ , with MCGs exhibiting rounder envelopes. Low- and high-ellipticity envelopes are broadly consistent with stellar halos and thick disks, respectively. However, the nature of intermediate ellipticity envelopes remains ambiguous from photometry alone. The coupling between component sizes, together with the survival of a substantial disk component, argues against dry minor mergers as the dominant envelope-building mechanism. A comparison with 8 relic galaxies reveals that MCGs and relics share similar bulge-disk-envelope structures and follow the same component size–mass relations, consistent with belonging to a common structural family.

**Keywords:** Early-type Galaxies (429); Compact galaxies (285); Galaxy stellar disks (1594); Galaxy bulges (578).

### 1. INTRODUCTION

In the local universe, galaxies are broadly divided into two main populations: the blue cloud, composed of star-forming galaxies in which stellar mass and star formation rate are tightly correlated (Brinchmann et al. 2004), and the red sequence, populated by quiescent galaxies whose star formation has been quenched. Observations at high redshift have shown that this color bimodality was already in place by  $z \sim 3$ , and that by  $z \sim 2$ , quiescent galaxies dominated the high-mass end of the stellar mass function (Davidzon et al. 2017). Compared to their local counterparts, these early quiescent systems were significantly more compact and often exhib-

ited stellar disks (van der Wel et al. 2014; Bundy et al. 2010; Davari et al. 2017). Similarly compact quiescent galaxies are rare in the local universe, implying substantial structural evolution of the quiescent population over the past  $\sim 10$  Gyr.

Two main mechanisms have been proposed to explain this evolution. The first is a two-phase scenario, in which individual compact quiescent galaxies grow through dry mergers (Naab & Ostriker 2009; Oser et al. 2010; Barro et al. 2013). The second is progenitor bias, whereby newly quenched galaxies are systematically larger because the sizes of star-forming progenitors increase with cosmic time (Carollo et al. 2013), thereby shifting the average properties of the quiescent population. Observations indicate that both effects contribute, with dry-merger growth becoming dominant at

$\log(M_*/M_\odot) \gtrsim 11.0$ , while progenitor bias plays an increasingly important role at lower masses (Fagioli et al. 2016; Williams et al. 2017; Damjanov et al. 2019). As a result, although the evolutionary path of the most massive compact quiescent galaxies is relatively well understood, that of intermediate- and lower-mass systems ( $\log(M_*/M_\odot) \lesssim 11.0$ ) remains less clear, since most low-redshift quiescent galaxies in this mass range quenched at later times, and only a small fraction are likely direct descendants of systems already in place at  $z \sim 2$ .

Studies of local ( $z \lesssim 0.2$ ) compact quiescent galaxies have revealed a mix of young and old systems (Ferré-Mateu et al. 2012; Jiang et al. 2012; Lasker et al. 2013; Yıldırım et al. 2017; Buitrago et al. 2018; Spiniello et al. 2021; Schnorr-Müller et al. 2021). They are typically fast rotators, consistent with dissipative formation followed by limited dry merging (Yıldırım et al. 2017; Schnorr-Müller et al. 2021). The oldest among them ( $\gtrsim 10$  Gyr), which exhibit kinematic and morphological properties consistent with passive evolution since  $z \sim 2$ , are classified as relic galaxies (Trujillo et al. 2014; Ferré-Mateu et al. 2015). However, searches for relic galaxies have traditionally focused on high-mass ( $\log M_*/M_\odot \gtrsim 10.8$ ), ultra-compact ( $R_e \lesssim 2$  kpc) systems, thereby probing only a small part of the region occupied by high-redshift quiescent galaxies in the  $\log M_*$ – $\log R_e$  plane. The intermediate-mass regime ( $10.0 \lesssim \log M_*/M_\odot \lesssim 10.8$ ) therefore remains largely unexplored.

To probe this less-studied regime, Schnorr-Müller et al. (2021) selected compact quiescent galaxies using a combination of stellar mass, velocity dispersion, and effective radius, adopting more relaxed criteria than the strict mass and size thresholds typically used in relic searches. Their sample included somewhat younger galaxies (median age  $\sim 8$  Gyr), but still metal-rich and  $\alpha$ -enhanced, suggesting that star formation was quenched after an intense early burst. Their kinematics revealed signatures of embedded stellar disks, indicating that quenching was followed by a merger-quiet phase. Crucially, they found that, at fixed stellar mass, older galaxies exhibit higher velocity dispersions, suggesting that the combination of compactness and high central velocity dispersion may be a more effective tracer of early quenching than compactness alone. Building on this result, Clerici et al. (2024) selected compact quiescent galaxies as  $+2\sigma$  outliers from the local stellar mass–velocity dispersion relation. These objects lie below the local size–mass relation—though not all are extremely compact—and are very old ( $\gtrsim 10$  Gyr), metal-rich, and  $\alpha$ -enhanced, with stellar population properties comparable to those of relic galaxies.

While the stellar population properties of relics, and compact quiescent galaxies in general, have been extensively studied, their morphological properties remain poorly constrained. Until recently, detailed morphological analyses were largely limited to a few case studies

(Jiang et al. 2012; Lasker et al. 2013; Yıldırım et al. 2015), which hinted at complex stellar structures not well captured by simple bulge–disk decompositions and requiring additional structural components. Building on these works, in the first paper of our series on the morphology of massive compact galaxies (Slodkowski Clerici et al. 2026, hereafter Paper I), we presented the results of a multi-component morphological decomposition of 245 massive compact galaxies, corresponding to a representative subset of the Clerici et al. (2024) sample. Our main finding was that massive compact galaxies are typically three-component systems, with compact bulges and disks embedded within an outer, lower-ellipticity envelope. In contrast, the majority of galaxies in a mass-matched control sample of early-type systems are well described by a bulge+disk model, with only a small fraction requiring an analogous three-component structure. The nature of the envelope remains unclear, but given its broad ellipticity range ( $\epsilon_{\text{Env}} \sim 0$ – $0.7$ ), it may correspond to a thick disk in some galaxies and to a stellar halo in others. In the absence of kinematic data, distinguishing between these possibilities requires constraining the intrinsic envelope ellipticity, which can only be done reliably in edge-on systems.

In this second paper of a series on the morphology of massive compact quiescent galaxies, we analyze a subset of 75 edge-on galaxies from the parent sample of Clerici et al. (2024) observed by the Hyper Suprime-Cam Subaru Strategic Program (HSC-SSP) imaging survey. Our goals are threefold: (i) to constrain the intrinsic envelope ellipticity and test the hypothesis that massive compact galaxies host thick disks and stellar haloes; (ii) to compare the structural properties of massive compact galaxies with those of three-component S0 galaxies of similar stellar mass, in order to identify how compact galaxies resemble and differ from their non-compact counterparts; and (iii) to test whether relic galaxies and massive compact galaxies can be considered part of the same structural family.

This paper is organized as follows. In Sec. 2, we describe the data and sample selection criteria. In Sec. 3, we present our multi-component decomposition strategy. Our results are shown and interpreted in Sec. 4, with further discussion in Sec. 5. Finally, we summarize our findings and present our conclusions in Sec. 6. Throughout this work, we adopt a simplified  $\Lambda$ CDM cosmology with  $\Omega_M = 0.3$ ,  $\Omega_\Lambda = 0.7$ , and  $H_0 = 70 \text{ km s}^{-1} \text{ Mpc}^{-1}$ .

## 2. DATA AND SAMPLE SELECTION

### 2.1. Massive Compact Galaxy Sample

The massive compact galaxy (hereafter MCG) sample studied in this work is drawn from the parent sample of Clerici et al. (2024). We briefly summarize its selection here and refer the reader to Clerici et al. (2024) for a detailed description. The parent sample was constructed from massive quiescent galaxies in the Sloan

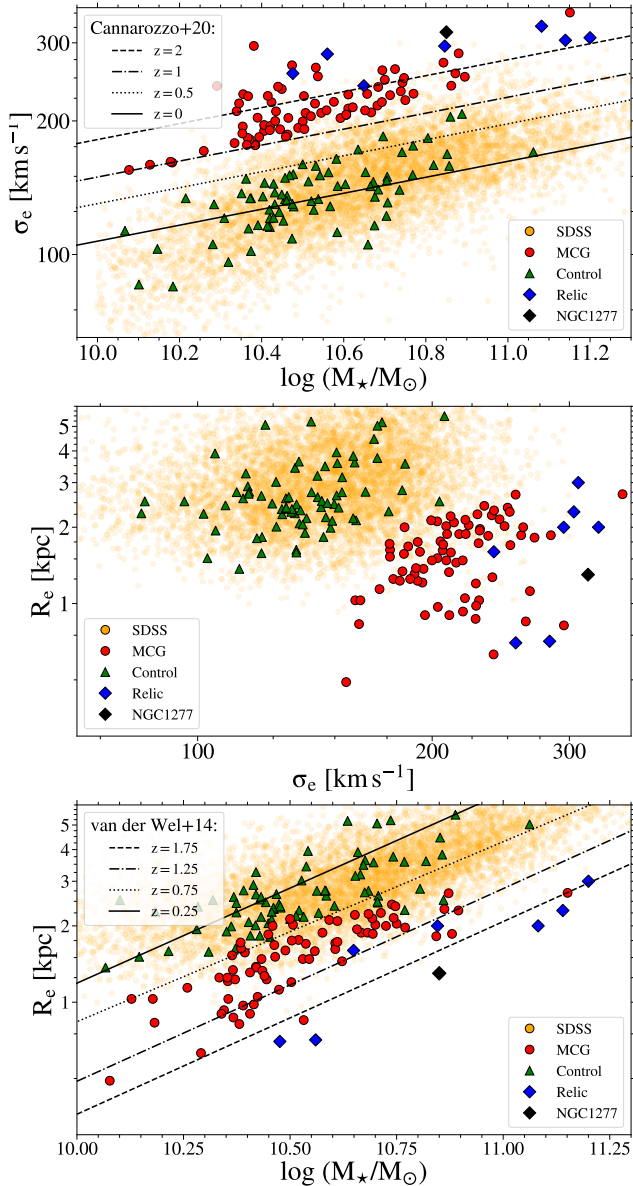


**Figure 1.** Sample selection. MCGs are shown as red circles, CSGs as green triangles, relic galaxies as blue diamonds (with the prototypical relic galaxy NGC 1277 highlighted as a black diamond) and SDSS quiescent edge-on S0 galaxies as orange circles. The top panel displays the stellar mass–velocity dispersion diagram, the middle panel shows the velocity dispersion–effective radius diagram, and the bottom panel presents the stellar mass–effective radius diagram. The top and bottom panels also include the stellar mass–velocity dispersion and size–mass relations at different redshifts.

Digital Sky Survey (SDSS) Data Release 14 (Abolfathi et al. 2018), selected to have  $\log(M_*/M_\odot) > 10$  and  $\log(\text{sSFR}/\text{yr}^{-1}) < -11$ . Linear fits were then performed to the stellar mass–velocity dispersion and velocity dispersion–effective radius relations. MCGs were

defined as galaxies lying more than  $+2\sigma$  above the stellar mass–velocity dispersion relation and more than  $-2\sigma$  below the velocity dispersion–effective radius relation, yielding a sample of 1858 galaxies at  $z < 0.1$ .

Stellar masses ( $M_*$ ) and star formation rates (SFR) were taken from the GALEX-SDSS-WISE Legacy Catalog (GSWLC; Salim et al. 2018). Effective radii ( $R_e$ ), defined as the semi-major axis of the half-light ellipse, were extracted from the catalog of Simard et al. (2011). Stellar velocity dispersions were retrieved from the SDSS spectroscopic catalog and converted to effective velocity dispersions ( $\sigma_e$ ) using the aperture correction relation  $\sigma_{\text{ap}} = \sigma_e [R_{\text{ap}}/R_e]^{-0.066}$  (Cappellari et al. 2006), where  $R_{\text{ap}}$  is the SDSS aperture radius.

Given their small sizes, characterizing the structure of MCGs requires imaging with higher spatial resolution than that provided by SDSS. The Hyper Suprime-Cam Subaru Strategic Program (HSC-SSP), a multi-band (*grizy*) imaging survey conducted with the Hyper Suprime-Cam (HSC) on the 8.2-meter Subaru Telescope (Aihara et al. 2018), provides an attractive alternative. Its wide layer covers  $\sim 1400 \text{ deg}^2$  to a depth of  $r \sim 26 \text{ mag}$ , with a median seeing of  $0.75''$  in the  $r$  band, and largely overlaps the SDSS footprint. A cross-match between the parent sample and the HSC-SSP source catalog yielded 245 matches. In the present study, we focus on the subset of HSC-observed MCGs with edge-on orientations, while an analysis of the full sample is presented in Paper I.

We identified edge-on MCGs from the multi-component decompositions of the HSC  $r$ -band images presented in Paper I. First, we selected galaxies for which a three-component model (Sérsic bulge + exponential disk + Sérsic envelope) was preferred over a two-component one, yielding a sample of 185 MCGs. We then visually inspected the HSC images to identify galaxies exhibiting disk isophotes, which are generally interpreted as signatures of highly inclined disks. Since the intrinsic thickness of the disk is unknown, the observed ellipticity cannot be directly converted into an inclination angle. Rather than restricting the sample exclusively to galaxies with clearly visible disk isophotes, we used these systems to determine an ellipticity threshold for highly inclined galaxies. This is because the prominence of disk isophotes depends not only on inclination, but also on the disk-to-total flux ratio, while point-spread function smearing can make compact flattened disks appear less elongated. As a result, some highly inclined systems are expected to exhibit only weakly disk isophotes and could therefore be missed in a purely visual classification. We found that galaxies exhibiting disk isophotes consistently have fitted disk ellipticities  $\geq 0.6$ , and therefore adopted this value as the threshold for selecting edge-on candidates. Applying this criterion yielded 89 galaxies. Of these, two were excluded due to heavy blending with nearby sources, two due to strong isophotal twists, one due to

a strongly warped disk, and two due to prominent outer star-forming rings. An additional seven galaxies were removed because the edge-on disk models provided poor fits. The final sample therefore consists of 75 edge-on MCGs.

### 2.2. Control Sample

To highlight how MCGs differ from non-compact S0 galaxies, we built a control sample of edge-on lenticular galaxies matched in stellar mass and redshift. In Paper I, we showed that central and satellite MCGs exhibit consistent morphological properties. We therefore restrict the control sample to central galaxies in order to exclude systems whose morphologies may have been significantly shaped by environmental processes acting exclusively on satellites.

We begin by selecting massive, quiescent lenticular galaxies ( $\log(M_*/M_\odot) > 10$ ,  $\log(\text{sSFR}/\text{yr}^{-1}) < -11$ , T-Type  $< 0$ ,  $P_{S0} > 0.7$ ) from a cross-match of the GSWLC, Simard et al. (2011), and Domínguez Sánchez et al. (2018) catalogs. Highly inclined candidates were identified using the probability of being edge-on ( $P_{\text{Edge-On}} > 0.7$ ). Galaxies were classified as centrals or satellites using the Lim et al. (2017) group catalog. After removing satellite galaxies, as well as  $+2\sigma$  outliers from the mass–velocity dispersion relation and  $-2\sigma$  outliers from the velocity dispersion–effective radius relation, we obtained a sample of 563 highly inclined S0 galaxies at  $z < 0.1$  with HSC imaging.

We then refined the sample by applying criteria analogous to those used for the MCGs. Two- and three-component models were fitted to all candidate galaxies, and the preferred model was selected using the same criteria adopted in Paper I. Galaxies for which a two-component model was preferred, as well as those with fitted disk ellipticities  $< 0.6$ , were excluded. It is worth noting that, unlike MCGs, many highly inclined S0s are adequately described by a two-component model, as shown in Paper I. For this reason we restrict the control sample to the subset of highly inclined S0s for which a three-component model is preferred. We further excluded galaxies with saturated centers, severe blending with nearby sources, strong isophotal twists, warped disks, or poor fits with the edge-on three-component model. This yielded a final pool of 155 highly inclined S0s. MCGs were then matched to these control galaxies in stellar mass and redshift using the MATCHIT R package (Ho et al. 2011) and the Propensity Score Matching (PSM) technique (Rosenbaum & Rubin 1983), resulting in a final matched sample of 75 edge-on S0s.

Figure 1 shows the distribution of MCGs and control sample galaxies (CSGs) in the stellar mass–velocity dispersion, velocity dispersion–effective radius, and stellar mass–effective radius diagrams. The top and bottom panels also include the stellar mass–velocity dispersion (Cannarozzo et al. 2020) and size–mass relations at different redshifts (van der Wel et al. 2014). Some overlap

**Table 1.** Properties of the relic galaxy sample. Asterisks denote stellar masses from Y17 converted to a Kroupa IMF.

| Name      | $\log(M_*/M_\odot)$ | $\sigma_e$<br>[km s <sup>-1</sup> ] | $R_e$<br>[kpc] | Inc.<br>[°] |
|-----------|---------------------|-------------------------------------|----------------|-------------|
| Mrk 1216  | 11.2*               | 308                                 | 3.0            | 70          |
| NGC 1270  | 11.1                | 327                                 | 2.0            | 80          |
| NGC 1271  | 10.8                | 295                                 | 2.0            | 83          |
| NGC 1277  | 10.8*               | 317                                 | 1.3            | 75          |
| NGC 1281  | 10.6                | 240                                 | 1.6            | 70          |
| PGC 12557 | 10.6                | 283                                 | 0.7            | 75          |
| PGC 12562 | 10.5                | 256                                 | 0.7            | 80          |
| PGC 32873 | 11.1*               | 304                                 | 2.3            | 84          |

exists in the stellar mass–effective radius plane, but excluding the overlapping galaxies does not significantly impact our results.

### 2.3. Relic Galaxy Sample

We define a second comparison sample composed of nearby galaxies previously classified as relics and for which archival *Hubble Space Telescope* (HST) imaging is available. Relic classifications were taken from Trujillo et al. (2014), Ferré-Mateu et al. (2015), and Ferré-Mateu et al. (2017). Nine relic galaxies have suitable HST imaging, however NGC 2767 was excluded because it exhibits a strong central position angle twist. For NGC 1277, we use F814W imaging from program GO:15235 (PI: W. E. Harris). For PGC 12557, we use F814W-WFC3 (Wide Field Camera 3) imaging from GO:14924 (PI: A. Seth). The remaining galaxies were observed in the near-infrared *H* band (F160W filter) with WFC3 as part of program GO:13050 (PI: R. van den Bosch).

The stellar masses, effective velocity dispersions, and effective radii of the relic galaxies are listed in Table 1. Stellar masses were taken from the GSWLC catalog when available, while the remaining galaxies have dynamically determined stellar masses from Yıldırım et al. (2017). Since GSWLC stellar masses assume a Kroupa initial mass function (IMF), we converted the Yıldırım et al. (2017) stellar masses using their published mass-to-light ratios to ensure consistency between the datasets. Effective radii and velocity dispersions were adopted from Yıldırım et al. (2017), except for PGC 12557, for which we use the values reported by Ferré-Mateu et al. (2015). Inclinations are also listed in Table 1. Yıldırım et al. (2017) provided inclination measurements for all galaxies except PGC 12557. Since a nuclear disk is clearly visible in the HST image of PGC 12557, we estimated its inclination from the observed disk geometry assuming an infinitely thin disk, obtaining 75°. Although not all relic galaxies in the

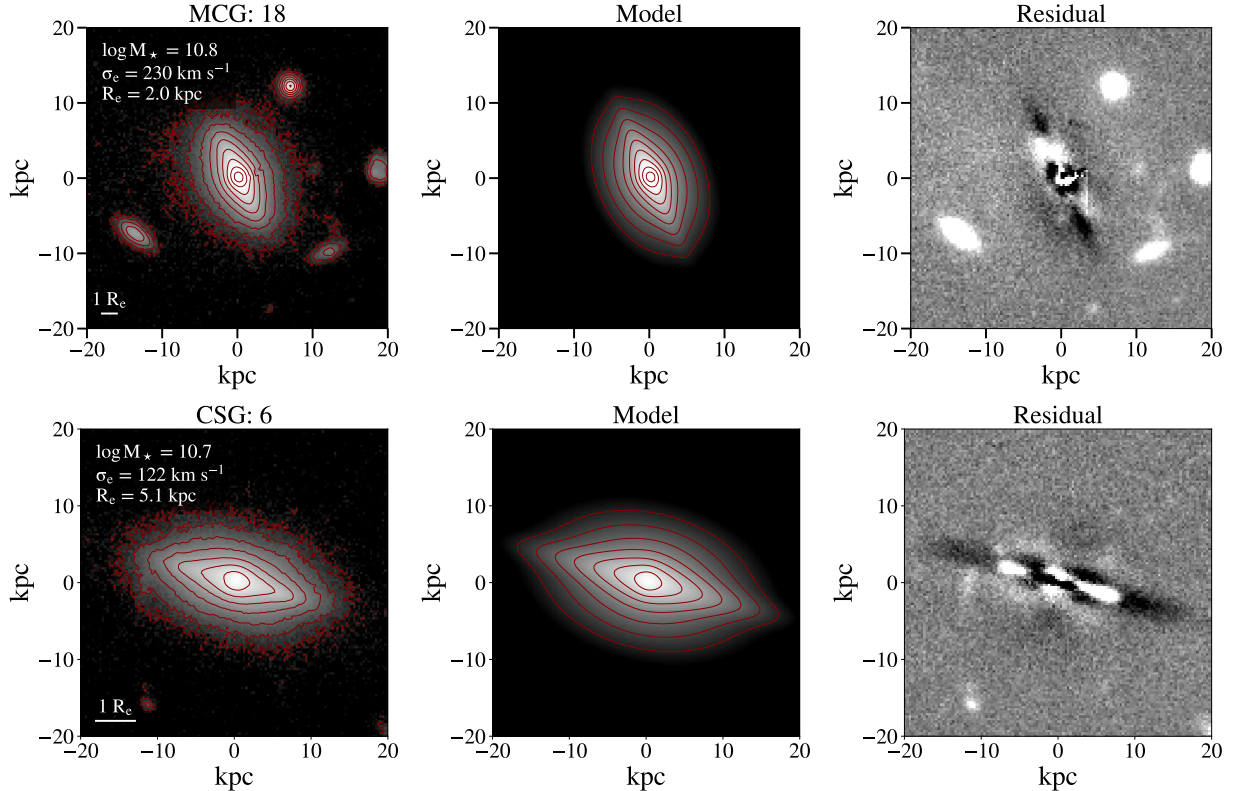


**Figure 2.**  $r$ -band image, best-fitting model, and residuals for an MCG (top) and a CSG (bottom). The image and model panels share the same logarithmic flux scale. The residuals are scaled separately to emphasize structural features.

sample are viewed exactly edge-on, all have inclinations  $> 70^\circ$ . This allows a structural analysis broadly comparable to that employed for the MCGs, requiring only minor adjustments to the fitting strategy, which are described in detail in the following section.

Relic galaxies are massive, compact, high-velocity-dispersion early-type systems. Their velocity fields exhibit regular rotation, and they host very old stellar populations ( $\gtrsim 13$  Gyr) out to a few  $R_e$ . In Fig. 1, relic galaxies are shown as blue diamonds, while the prototypical relic galaxy NGC 1277 is highlighted as a black diamond. As can be seen, relic galaxies satisfy the stellar mass, size, and velocity-dispersion criteria used to select MCGs.

### 3. MULTI-COMPONENT DECOMPOSITION STRATEGY

We modeled the surface brightness distributions of the galaxies using IMFIT (Erwin 2015), which includes both standard image functions, such as the Sérsic profile, and 3D luminosity-density models integrated along the line of sight, particularly useful for fitting highly inclined disks. The required inputs for IMFIT are a galaxy image, an associated noise map, a point-spread function (PSF), a mask image, and a configuration file specifying the model components, together with the free and fixed parameters, their bounds, and their initial values.

IMFIT provides three different  $\chi^2$  minimization methods: the Levenberg–Marquardt algorithm, the Nelder–Mead simplex method, and differential evolution. We adopted the differential evolution algorithm because it does not require initial guesses for the fitted parameters, relying instead on user-defined lower and upper bounds, and is less prone to becoming trapped in local minima than the alternative optimizers available in IMFIT. It has also been shown to yield robust results with minimal user intervention (see Gadotti 2026 for a detailed discussion). Parameter bounds were defined following the strategy described in Paper I.

For the MCG and control samples, the PSF and variance maps were provided by the HSC pipeline (Bosch et al. 2018). For the relic galaxy sample, we constructed empirical effective point-spread functions (ePSFs), which account for both the telescope PSF and detector sampling, using bright, isolated stars in the corresponding HST fields. The ePSFs were generated with the EPSFBUILDER module from the astropy Python package, following the methodology described by Anderson & King (2000) and Anderson (2016). Mask images were created from segmentation maps produced with SEXTRACTOR (Bertin & Arnouts 1996), with all pixels not associated with the target galaxy masked out.

### 3.1. MCG and CSG Samples

Each galaxy was modeled with three components: an inner Sérsic bulge, an edge-on disk, and a Sérsic envelope. The projected intensity distribution of the edge-on disk component is defined in cylindrical coordinates as:

$$I(r, z) = \mu_0 \frac{r}{h_R} K_1 \left( \frac{r}{h_R} \right) \operatorname{sech}^{2/\alpha} \left( \frac{z}{2z_0} \right), \quad (1)$$

where  $h_R$  is the scale length,  $z_0$  is the scale height,  $K_1$  is the modified Bessel function of the second kind,  $\mu_0$  is the central surface brightness, and  $\alpha$  controls the shape of the vertical profile. This expression corresponds to the projected intensity distribution of a perfectly edge-on disk with an exponential radial profile, using the Bessel-function solution of van der Kruit & Searle (1981) for the radial dependence. We adopt a  $\operatorname{sech}^2$  vertical profile (i.e.,  $\alpha = 1$ ), corresponding to the solution for a self-gravitating isothermal sheet (Spitzer 1942).

The disk model includes four free parameters: position angle ( $PA_{\text{disk}}$ ), central surface brightness ( $\mu_0$ ), radial scale length ( $h_R$ ), and vertical scale height ( $z_0$ ). The bulge and envelope are each modeled with a Sérsic profile defined by their position angle, ellipticity, effective radius, and intensity at the effective radius. The Sérsic index  $n$  is treated as a free parameter for the bulge, but fixed to  $n = 1$  for the envelope in order to limit model complexity, since allowing it to vary yields comparable  $\chi^2$  values and variations of typically only a few percent in the envelope parameters. For most galaxies, the bulge effective radius is smaller than half the PSF full width at half maximum (FWHM). We therefore tested replacing the bulge Sérsic profile with a point-source model, implemented as a scaled version of the user-supplied PSF. This substitution consistently produced poorer fits, reinforcing our decision to model the bulge with a Sérsic profile despite the limited spatial resolution.

Nine MCGs required an additional outer low-ellipticity ( $\epsilon \sim 0$ ) exponential component to adequately reproduce both the surface-brightness distribution and the radial variation of ellipticity in their outskirts. In these cases, the residual maps of the three-component fits showed significant large-scale residual structures with a rounder spatial distribution. Allowing the envelope Sérsic index to vary freely was insufficient to reproduce these features, requiring the inclusion of an additional low-ellipticity exponential component. Since it is unclear whether the envelope component in these galaxies has the same physical nature as the envelope identified in galaxies well described by a three-component model, these systems were excluded from all envelope-related plots and from the computation of median envelope properties.

All galaxies were fit using  $40 \text{ kpc} \times 40 \text{ kpc}$  image cutouts. An example fit is shown in Fig. 2. The overlaid isophotes demonstrate that our model successfully reproduces the disk isophotes near the mid-plane as well

as the more elliptical isophotes at larger vertical distances. However, the modeled disk isophotes extend to larger radial distances than observed. This discrepancy arises because the disk flares, and our modeling approach does not account for this effect.

Finally, one potential source of systematic uncertainty is the comparison between the optical  $r$ -band HSC images of MCGs and the near-infrared  $H$ -band HST images of relic galaxies, since morphological parameters are known to vary with wavelength. However, multi-component morphological decompositions of  $z$ -band HSC images yield changes of only a few percent in the derived parameters compared to the  $r$ -band images adopted as the default. This indicates that any wavelength-dependent bias in our analysis is negligible.

The full table containing the galaxy properties and structural parameters derived from our multi-component photometric decompositions of the MCG and CSG samples will be made available in machine-readable format through Vizier upon publication of this paper.

### 3.2. Relic Galaxy Sample

Fitting the relic galaxies required minor adjustments to our fitting strategy. First, since inclination estimates are available for each relic galaxy, we replaced the perfectly edge-on disk model with a 3D disk luminosity-density model projected onto the plane of the sky at the adopted inclination. The 3D disk luminosity density is given by

$$j(r, z) = J_0 \exp \left( -\frac{r}{h_R} \right) \operatorname{sech}^{2/\alpha} \left( \frac{z}{2z_0} \right), \quad (2)$$

where  $r$  and  $z$  are cylindrical coordinates aligned with the disk. The free parameters of the 3D disk model are the position angle ( $PA_{\text{disk}}$ ), central luminosity density ( $J_0$ ), radial scale length ( $h_R$ ), and vertical scale height ( $z_0$ ). As in the edge-on disk model, we adopt  $\alpha = 1$ , corresponding to a  $\operatorname{sech}^2$  vertical profile.

Second, Mrk 1216, NGC 1270, NGC 1271, and PGC 32873 exhibit boxy envelopes surrounding their disks. For these galaxies, we modeled the envelope using the *SérsicGenEllipse* function within IMFIT, which generalizes the standard Sérsic profile by allowing non-elliptical isophotes through an additional parameter,  $c_0$  ( $c_0 > 0$  for boxy,  $c_0 < 0$  for disk, and  $c_0 = 0$  for purely elliptical isophotes).

Third, the same four galaxies required an additional outer round component ( $\epsilon \sim 0$ ) to achieve satisfactory fits. These structures were modeled with an exponential component.

Fourth, owing to their small distances and the high spatial resolution of the HST images, most relic galaxies exhibit substructures within the photometric bulge, such as nuclear stellar and/or dust disks and bright nuclear point sources. Modeling or masking these struc-

tures does not significantly affect the bulge ellipticity or effective radius measurements, although  $n_{\text{bulge}}$  is substantially impacted. To identify such components, we visually inspected both the galaxy images and the residual maps from the three- (or four-) component fits. Bright nuclear point sources are present in NGC 1270, NGC 1281, PGC 12562, and PGC 32873, and were modeled using a PointSource function. We also repeated the fitting process while masking the nuclear disks in NGC 1277, NGC 1281, PGC 12557, PGC 12562, and PGC 32873. NGC 1270 exhibits an edge-on nuclear disk but no large-scale edge-on disk; in this case, we treat the nuclear disk as the main galaxy disk. Accounting for these substructures decreases  $n_{\text{bulge}}$  by up to  $\sim 20\%$  relative to fits in which they are ignored.

## 4. RESULTS

### 4.1. Morphological Properties of MCGs and CSGs

Figure 3 presents the morphological properties and flux-to-total ratios of the different structural components. Throughout this paper, we consider differences between distributions to be statistically significant when the Kolmogorov–Smirnov test yields  $p < 0.05$ . The first row shows the effective radius, Sérsic index, and ellipticity of the bulges. A comparison of the effective radius distributions ( $R_{e,\text{Bulge}}$ ) shows that the bulges of MCGs are significantly more compact, with 65% having  $R_{e,\text{Bulge}} < 400$  pc, compared to only 24% in the control sample, although this result should be interpreted with caution given the resolution limit of the HSC data; for all MCGs,  $R_{e,\text{Bulge}}$  is smaller than the full width at half maximum of the PSF and should therefore be regarded as an upper limit. This limitation is also reflected in the Sérsic index and ellipticity distributions: MCGs cluster near the boundaries of the allowed parameter space—toward the lower bound in  $n$  and the upper bound in  $\epsilon_{\text{Bulge}}$ —indicating that these parameters are driven by the fitting limits and are thus poorly constrained.

To assess the reliability of our  $R_{e,\text{Bulge}}$  measurements, we searched for *HST* archival observations of the parent MCG sample. Of the 1858 MCGs in the Clerici et al. (2024) sample, 15 have available data, four of which satisfy our edge-on criteria. Details of these observations and their multi-component decompositions are provided in Appendix A. Briefly, for one galaxy the bulge is best fit by a point source, consistent with  $R_{e,\text{Bulge}} \lesssim 200$  pc, while the other three have  $R_{e,\text{Bulge}} \sim 0.15\text{--}0.35$  kpc,  $\epsilon_{\text{Bulge}} \sim 0.2\text{--}0.5$ , and  $n_{\text{Bulge}} \sim 2$ . Overall, the *HST*-based sizes are comparable to those measured from the HSC images, suggesting that the  $R_{e,\text{Bulge}}$  distribution is broadly reliable, even though individual measurements remain uncertain. Given the above, we adopt  $R_{e,\text{Bulge}}$  as the primary bulge structural parameter throughout the remainder of this paper, and defer the analysis of Sérsic indices and bulge ellipticities to future work with higher-resolution data.

The second row of Fig. 3 displays the scale length, scale height, and scale-length-to-height ratio ( $h_r/z_0$ ) of the edge-on disk component. MCG disks are generally more compact, with 77% having radial scale lengths  $h_r < 1.5$  kpc, compared to only 31% of control S0s. They also tend to have smaller vertical scale heights, with median values of  $z_0 \sim 0.29$  kpc for MCGs and  $z_0 \sim 0.38$  kpc for CSGs, although this difference is less pronounced than that in scale length and the distributions overlap significantly. The difference between the distributions is primarily driven by the high- $z_0$  tail: 40% of control S0s have  $z_0 > 0.4$  kpc, whereas only 17% of MCGs exceed this value. The  $h_r/z_0$  distribution further highlights the structural differences, with MCGs showing systematically lower ratios: 84% have  $h_r/z_0 < 5$ , compared to 44% of control galaxies. This indicates that, although MCGs have smaller scale heights on average, their even shorter radial scale lengths result in disks that are proportionally thicker.

In the third row of Fig. 3, we present the distributions of envelope ellipticity and effective radius. As seen for the bulge and disk components, MCG envelopes are typically more compact. Although the ellipticity ranges overlap, their distributions differ markedly: MCGs preferentially host rounder envelopes, with 72% having  $0.2 < \epsilon_{\text{Envelope}} < 0.5$ , compared to only 25% of CSGs. Conversely, 73% of CSGs have  $\epsilon_{\text{Envelope}} > 0.5$ , versus only 19% among MCGs.

The fourth row of Fig. 3 displays the flux-to-total ratios of the bulge, disk, and envelope components. The median  $B/T$  ( $\sim 26\%$ ),  $D/T$  ( $\sim 42\%$ ), and  $Env/T$  ( $\sim 30\%$ ) values are similar between the samples. In the majority of galaxies the disk contributes the largest fraction of the total flux (69% of MCGs and 60% of CSGs). In contrast, the fraction of galaxies in which the bulge contributes the largest fraction of the total flux is low, at  $\sim 10\%$  in both samples.

### 4.2. Morphological properties of Relic Galaxies

Table 2 lists the morphological parameters of the eight relic galaxies analyzed in this work, along with the median values for MCGs for comparison. Relic galaxies share several structural characteristics with MCGs: they host compact bulges ( $R_{e,\text{Bulge}} \sim 0.3\text{--}0.9$  kpc), and their disks are short ( $h_R \sim 0.5\text{--}2$  kpc), thick ( $h_R/z_0 \sim 2\text{--}7$ ), and embedded within flattened stellar envelopes ( $\epsilon_{\text{Envelope}} \sim 0.2\text{--}0.7$ ). Four relic galaxies required an additional outer component to achieve satisfactory fits. Given its low ellipticity ( $\epsilon_h \sim 0\text{--}0.3$ ), we interpret this fourth component as a stellar halo. We note that only nine MCGs required a similar fourth component. It remains unclear whether such four-component structures are intrinsically rarer among MCGs or simply go undetected due to the depth limitations of the HSC data.

In Fig. 4, we compare images of relic galaxies and MCGs. The top panels show three relic galaxies, while the bottom panels present three MCGs selected to have

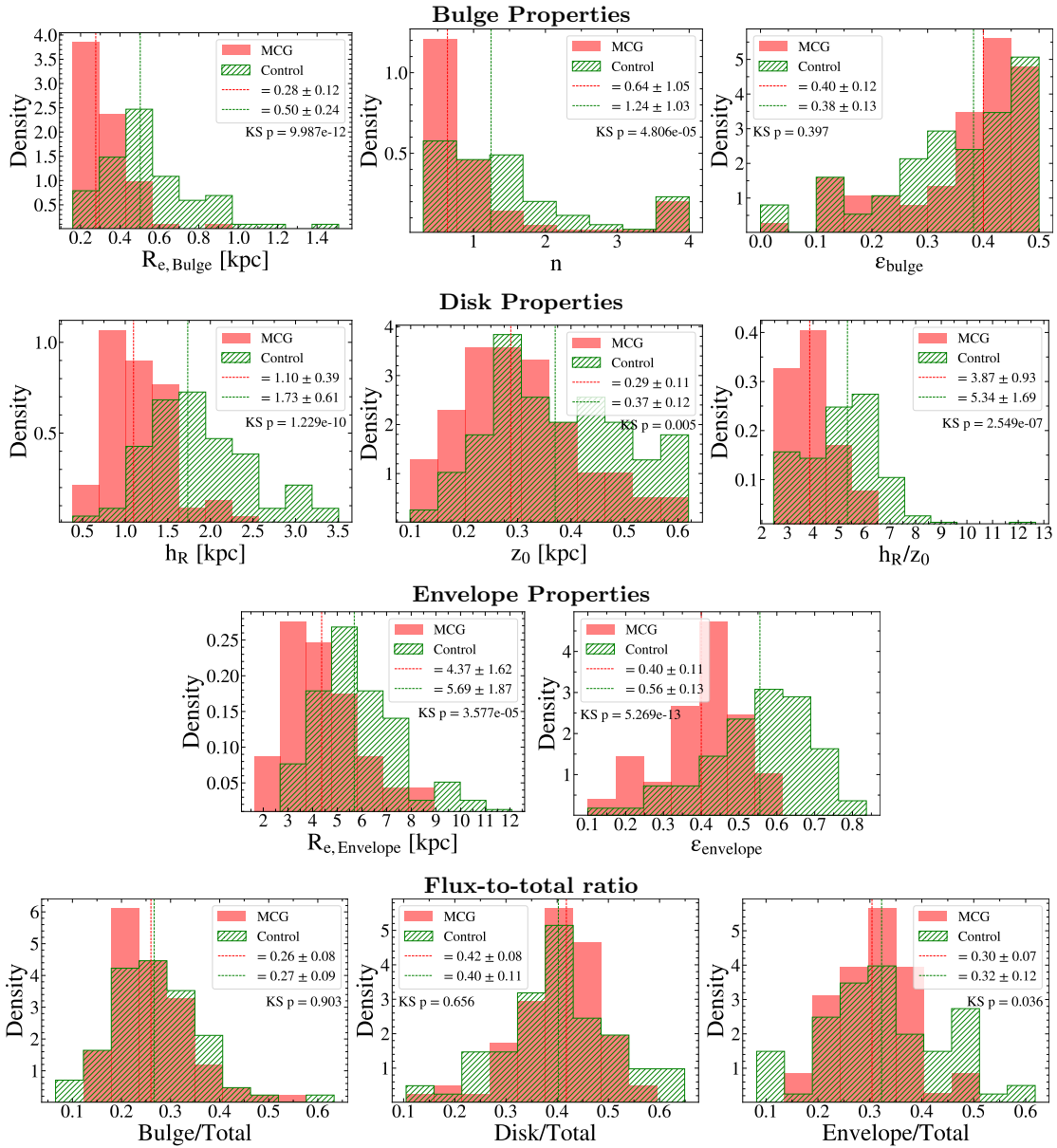


**Figure 3.** Structural properties of MCGs and CSGs. The first row shows the effective radius, Sérsic index and ellipticity of the bulge component. The second row presents the disk scale length, scale height, and the ratio between them. In the third row, we show the effective radius and ellipticity of the stellar envelope, modeled with a fixed Sérsic index of  $n = 1$ . The fourth row displays the flux-to-total ratio of each component. Dashed lines indicate the median values for each sample. Galaxies best fitted with a four-component model were excluded from the histograms of the envelope properties.

similar stellar masses, effective radii, and velocity dispersions. It is evident from the images that MCGs and relic galaxies are morphologically very similar. However, inspection of the structural parameters in Table 2 reveals a few significant differences. Notably, relic galaxies have larger B/T ratios. Additionally, five out of eight relics have  $D/T \lesssim 0.15$ . Conversely, no MCGs show similarly low  $D/T$  values.

Although the small sample size precludes firm conclusions, these differences raise some possibilities. One is that our sample is biased toward systems with higher

$D/T$  ratios due to the selection criteria: galaxies with low  $D/T$  may not display sufficiently disk-like isophotes to be well described by our three-component model and would therefore be excluded from the sample. Alternatively, galaxies with lower  $D/T$  ratios may simply become more common at  $\log(M_*/M_\odot) \gtrsim 11$ , a stellar-mass regime represented by only one MCG in our current sample.

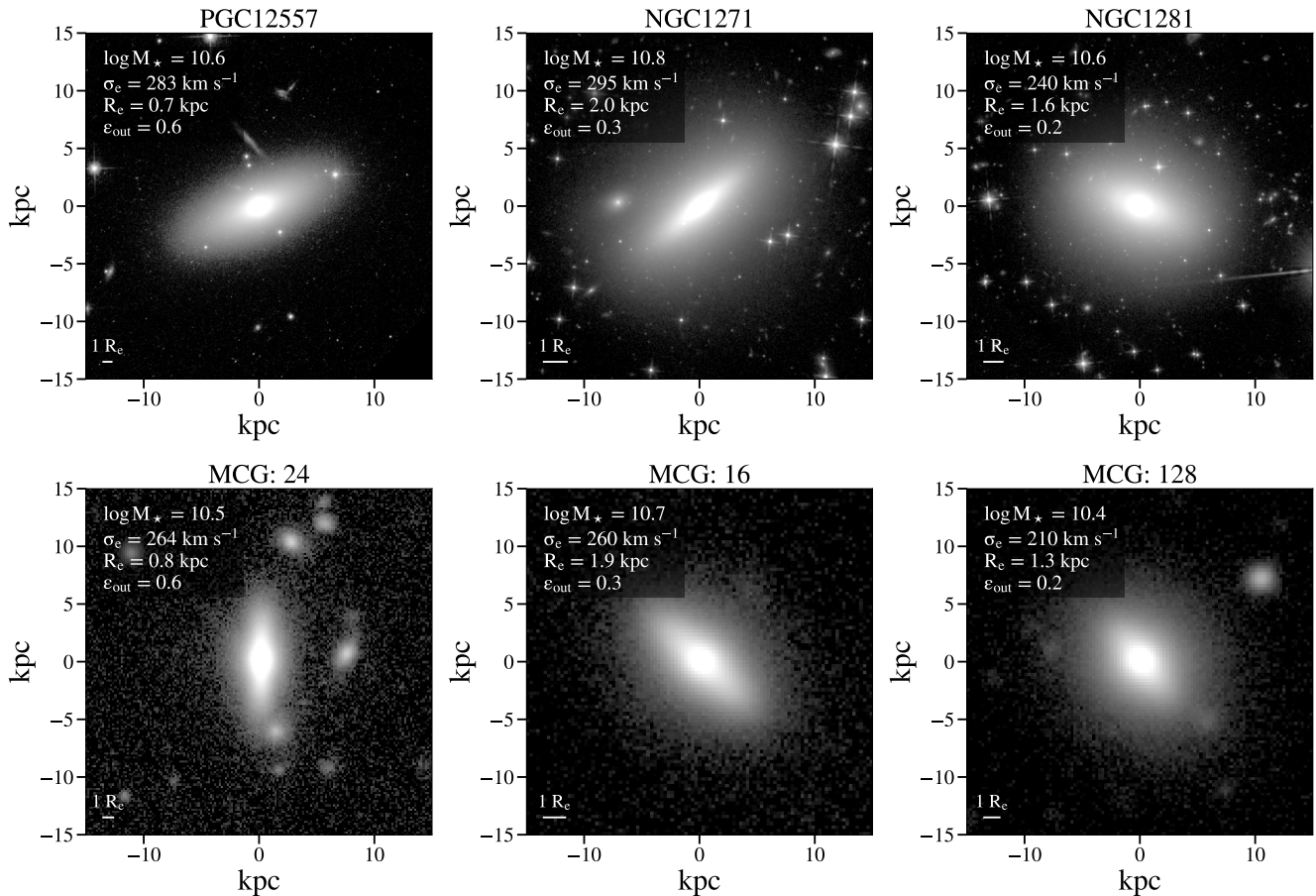


**Figure 4.** A comparison between relic galaxies and MCGs. The top panels displays HST images of three relic galaxies, while the bottom panel shows MCGs with similar stellar mass, velocity dispersion, effective radius, and ellipticity of the outermost component. The morphological similarity between relics and MCGs is clear.

#### 4.3. Size-mass Relations of the Bulge, Disk, and Envelope

In Fig. 5, we show the mass–size relations for bulges, disks, and envelopes, along with the disk mass–scale height relation. MCGs, relics, and CSGs are shown as red circles, blue diamonds, and green triangles, respectively. Given the similar distributions of MCGs and relics, we perform a combined fit to these two populations, indicated by the dashed red line, while the dashed green line shows the best fit to the CSG distribution. Reference relations from local and high-redshift samples are also included.

The top-left panel shows the bulge mass–size relation. Compared to MCGs, CSGs are shifted to larger bulge sizes at fixed stellar mass, although there is some overlap between the samples at the low-mass end. Relics mainly occupy the high-mass end, extending the MCG trend toward larger masses and sizes. Compared to best-fitting relations from the literature, the MCG fit lies close to the quenched bulge relation at  $1.0 < z \leq 1.5$  (Nedkova et al. 2024), but due to its different slope, it lies above that relation at  $\log(M_*/M_\odot) \sim 10.3$  and below it at higher masses. Notably, relic galaxies tend to fall on or

below the Nedkova et al. (2024) relation, whereas MCGs exhibit a broader spread, likely reflecting the resolution limits of the HSC data. The CSG fit has a similar slope to the Nedkova et al. (2024) and Cook et al. (2025) relations, lying between them.

The top-right panel shows the disk mass–scale length relation. The best-fitting relations for MCGs and CSGs have similar slopes. When compared to size–mass relations from the literature (converted to  $h_R$  using  $R_e = 1.678 h_R$  for an exponential disk), both MCG and CSG disks appear more compact than the thin disks of  $z \sim 0.1 - 2$  star-forming galaxies (Tsukui et al. 2025) and the disks of local early-type galaxies (Lange et al. 2016). Moreover, MCG disks are also shorter than those of  $z \sim 1$  quenched galaxies (Nedkova et al. 2024) and galaxies hosting classical bulges (Cook et al. 2025). Notably, the MCG relation differs from these not only in zero point but also in slope, showing a stronger mass dependence. Relic disks have comparable sizes and stellar masses to MCG disks. However, as relics tend to host more massive bulges at fixed total stellar mass, their disks and envelopes carry a smaller fraction of the total mass. Since component sizes scale with component

**Table 2.** Structural parameters and flux-to-total ratios for relic galaxies. Median values and standard deviations are given for relics and MCGs for comparison. Standard deviations for the halo component are not shown due to small number of objects requiring a fourth component. Columns: bulge ellipticity ( $\epsilon_{\text{bulge}}$ ), Sérsic index ( $n_{\text{bulge}}$ ), bulge effective radius ( $R_{e,\text{bulge}}$  [kpc]), bulge-to-total ratio (B/T), disk radial scale length ( $h_R$  [kpc]), vertical scale height ( $z_0$  [kpc]), scale length-to-height ratio ( $h_R/z_0$ ), disk-to-total ratio (D/T), envelope ellipticity ( $\epsilon_{\text{env}}$ ), envelope effective radius ( $R_{e,\text{env}}$  [kpc]), envelope-to-total ratio (Env/T), halo ellipticity ( $\epsilon_{\text{halo}}$ ), halo effective radius ( $R_{e,\text{halo}}$  [kpc]), and halo-to-total ratio (Halo/T). Ellipticities were converted from observed to intrinsic assuming each component is well described by an axisymmetric oblate spheroid. Galaxies best fitted with a four-component model were excluded from the computation of the median and standard deviation of envelope structural parameters.

| Name            | $\epsilon_{\text{bulge}}$ | $n_{\text{bulge}}$ | $R_{e,\text{bulge}}$<br>[kpc] | B/T  | $h_R$<br>[kpc] | $z_0$<br>[kpc] | $h_R/z_0$ | D/T  | $\epsilon_{\text{env}}$ | $R_{e,\text{env}}$<br>[kpc] | Env/T | $\epsilon_{\text{halo}}$ | $R_{e,\text{halo}}$<br>[kpc] | Halo/T |
|-----------------|---------------------------|--------------------|-------------------------------|------|----------------|----------------|-----------|------|-------------------------|-----------------------------|-------|--------------------------|------------------------------|--------|
| Mrk1216         | 0.4                       | 2.3                | 0.42                          | 0.25 | 0.7            | 0.16           | 4.5       | 0.08 | 0.6                     | 3.1                         | 0.32  | 0.0                      | 8.2                          | 0.35   |
| NGC1270         | 0.3                       | 1.7                | 0.87                          | 0.39 | 0.1            | 0.06           | 2.3       | 0.05 | 0.4                     | 3.3                         | 0.19  | 0.0                      | 5.2                          | 0.37   |
| NGC1271         | 0.4                       | 2.2                | 0.25                          | 0.25 | 0.9            | 0.13           | 7.0       | 0.12 | 0.7                     | 2.5                         | 0.38  | 0.3                      | 4.5                          | 0.25   |
| NGC1277         | 0.4                       | 1.5                | 0.41                          | 0.35 | 1.0            | 0.28           | 3.6       | 0.20 | 0.6                     | 3.1                         | 0.44  | –                        | –                            | –      |
| NGC1281         | 0.4                       | 1.2                | 0.37                          | 0.29 | 1.3            | 0.33           | 3.8       | 0.32 | 0.2                     | 3.2                         | 0.38  | –                        | –                            | –      |
| PGC12557        | 0.2                       | 1.9                | 0.34                          | 0.41 | 0.6            | 0.12           | 5.3       | 0.16 | 0.6                     | 2.7                         | 0.44  | –                        | –                            | –      |
| PGC12562        | 0.3                       | 1.7                | 0.37                          | 0.49 | 1.1            | 0.34           | 3.4       | 0.31 | 0.6                     | 3.8                         | 0.20  | –                        | –                            | –      |
| PGC32873        | 0.3                       | 2.0                | 0.68                          | 0.42 | 2.0            | 0.45           | 4.4       | 0.10 | 0.6                     | 4.9                         | 0.32  | 0.3                      | 13.9                         | 0.16   |
| Median (Relics) | 0.35                      | 1.8                | 0.39                          | 0.37 | 0.9            | 0.20           | 4.1       | 0.14 | 0.58                    | 3.2                         | 0.41  | 0.15                     | 6.7                          | 0.30   |
| Std dev         | 0.06                      | 0.3                | 0.21                          | 0.08 | 0.5            | 0.14           | 2.8       | 0.10 | –                       | –                           | –     | –                        | –                            | –      |
| Median (MCGs)   | –                         | –                  | 0.28                          | 0.26 | 1.1            | 0.29           | 3.9       | 0.42 | 0.40                    | 4.4                         | 0.30  | 0.15                     | 7.0                          | 0.23   |
| Std dev         | –                         | –                  | 0.12                          | 0.08 | 0.4            | 0.11           | 0.9       | 0.08 | 0.11                    | 1.6                         | 0.07  | –                        | –                            | –      |

mass, this naturally explains why relics are more compact than MCGs at fixed total stellar mass: higher  $B/T$  ratios reduce galaxy sizes not only through the larger bulge contribution, but also because less massive disks and envelopes are intrinsically smaller.

The bottom-left panel shows the envelope mass–size relation. Both samples display considerable scatter, particularly the CSGs, but MCG envelopes are typically more compact. The MCG relation shows a stronger mass dependence and converges toward the CSG trend at higher masses. As one possible interpretation is that the envelope corresponds to a thick disk, we compare its mass–size relation to that of thick disks in star-forming galaxies (Tsukui et al. 2025), finding that most envelopes lie below this relation.

The bottom-right panel shows the disk scale height as a function of mass. In contrast to the disk scale length, MCGs and CSGs do not show a clear separation in scale height, with the two samples largely overlapping. Consequently, given their shorter scale lengths, MCG disks are proportionally thicker. Compared to the scale height–stellar mass relation of star-forming galaxies (Tsukui et al. 2025), the disk scale heights of MCGs show a stronger mass dependence.

#### 4.4. Coupling of Component Lengths

S0 and spiral galaxies display a coupling between  $R_{e,\text{bulge}}$  and  $h_R$ , which has been interpreted as evidence that the formation processes of these components are linked (Aguerri et al. 2005; Carollo et al. 2007; Noordermeer & van der Hulst 2007; Laurikainen et al. 2009, 2010). To test whether a similar coupling is present in MCGs, we show in the top panel of Fig. 6  $R_{e,\text{bulge}}$  as

a function of  $h_R$ . The dashed lines indicate linear fits to the CSG (green) and the combined MCG+relic (red) distributions. A coupling is present, with Spearman correlation coefficients of  $r = 0.72$  for MCGs and  $r = 0.62$  for CSGs.

To test whether a similar coupling is present between the disk and the envelope, we show in the bottom panel of Fig. 6  $h_R$  as a function of  $R_{e,\text{Envelope}}$ . A correlation is clearly present, with Spearman coefficients of  $r = 0.69$  for MCGs and  $r = 0.48$  for CSGs. The presence of this coupling suggests a relatively quiet post-quenching accretion history in MCGs, as repeated dry minor mergers are expected to disrupt both the disk and the envelope, thereby weakening or erasing this relation, and only gas-rich mergers could plausibly re-establish it (Querejeta et al. 2015).

## 5. DISCUSSION

### 5.1. Insights into the Formation of MCGs from the Disk Structure

The comparison between the disk scale lengths and scale heights of MCGs and CSGs shown in Figs. 3 and 5 offers valuable insight into the conditions under which the disks of MCGs formed. The scale height of a self-gravitating isothermal sheet is given by  $z_0 = \sigma_*^2 / (2\pi G \Sigma_*)$  (Binney & Tremaine 2008), where  $\sigma_*$  and  $\Sigma_*$  are the stellar velocity dispersion and stellar surface density, respectively. Since the  $z_0$  distributions of MCGs and CSGs largely overlap, while MCG disks are systematically shorter at fixed stellar mass (and therefore denser), the disks of MCGs are expected to have higher  $\sigma_*$ . If stellar disks preserve, at least partially, the kinematic properties of the gas disks in which they formed,

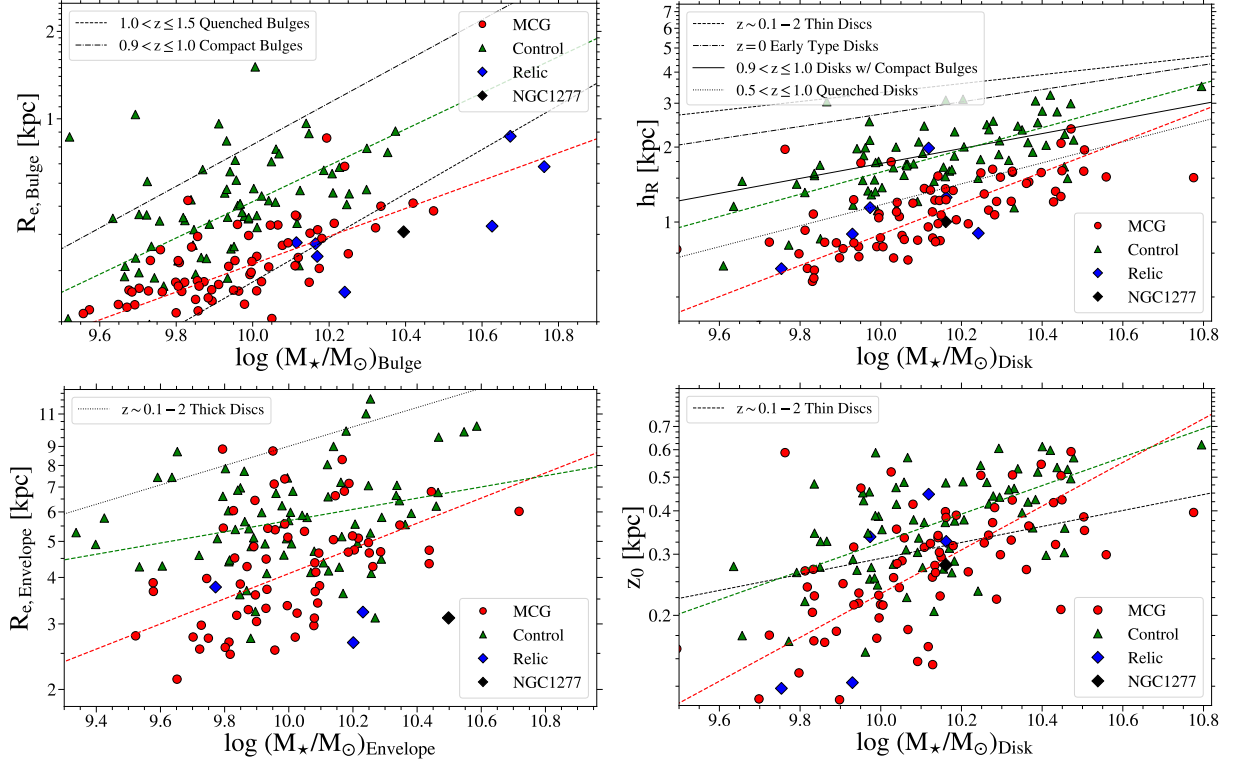


**Figure 5.** Size–mass relations for the bulge (top left), disk (top right), and envelope (bottom left), together with the scale height–disk mass relation (bottom right). MCGs are shown as red circles, CSGs as green triangles, and relic galaxies as blue diamonds, with the prototypical relic galaxy NGC1277 highlighted as a black diamond. Best-fit relations from the literature for local and high-redshift galaxies are overplotted in each panel for comparison. The dashed red line shows a linear fit to the combined MCG and relic galaxy distribution, while the dashed green line indicates the best fit to the CSG distribution. Galaxies best fitted with a four-component model are excluded from the envelope size–mass relation.

this suggests that the star-forming progenitors of MCGs hosted more turbulent gas disks than the progenitors of CSGs. An evolutionary connection between MCGs and compact high-redshift starbursts provides a possible explanation for this scenario, since intensely star-forming dust-obscured galaxies at  $z \sim 1.3\text{--}2.6$  have been found to exhibit elevated  $H\alpha$  velocity dispersions compared to less actively star-forming galaxies at similar redshifts (Birkin et al. 2024). It is worth noting that the stellar population properties of MCGs, namely their old ages, supersolar metallicities, and enhanced  $[\alpha/\text{Fe}]$  reported by Clerici et al. (2024), are also consistent with such an evolutionary connection.

## 5.2. The Nature of the Envelope

An extended stellar envelope surrounds the disks of MCGs, containing  $\sim 25\%$  of the total flux. The envelope ellipticity ranges from 0.0 to 0.6, with a median value of  $\epsilon_{\text{env}} \sim 0.4$ . This suggests that in some cases the envelope corresponds to a stellar halo, while in others it is more consistent with a thick disk. Although the nature of the envelope cannot be determined unambiguously without spatially resolved kinematics, examining MCGs at the extremes of the ellipticity distribution provides valuable insight into its origin.

We first consider MCGs with low envelope ellipticity ( $\epsilon_{\text{env}} < 0.3$ ), which account for 17% of the sample. Two representative examples, MCGs ID 25 and 220, are shown in the top panels of Fig. 7. Galaxies in this group exhibit compact disks embedded within round stellar envelopes. They resemble compact analogs of the halo-embedded disk galaxies identified in IllustrisTNG50 by Du et al. (2021) and He et al. (2025), which consist of intermediate-scale disks surrounded by diffuse stellar halos. Du et al. (2021) proposed an evolutionary scenario in which a major merger disrupts an early disk and builds a stellar halo, followed by disk regrowth through residual star formation fueled by leftover gas after coalescence. A similar mechanism may apply to some MCGs, provided the merger occurred at  $z \gtrsim 2$ , consistent with their old stellar populations (see Clerici et al. 2024). In this scenario, the disk-dominated structure of low- $\epsilon_{\text{env}}$  MCGs (D/T  $\sim 0.4$ , Env/T  $\sim 0.2$ ) may reflect the high gas fractions expected at early cosmic times, which favor efficient disk regrowth post-merger.

A similar conclusion can be drawn by comparing MCGs and relic galaxies. In a recent study, Zhu et al. (2025) analyzed the dynamical properties of compact early-type galaxies in IllustrisTNG50 and classified them as “merger-free” or not based on whether

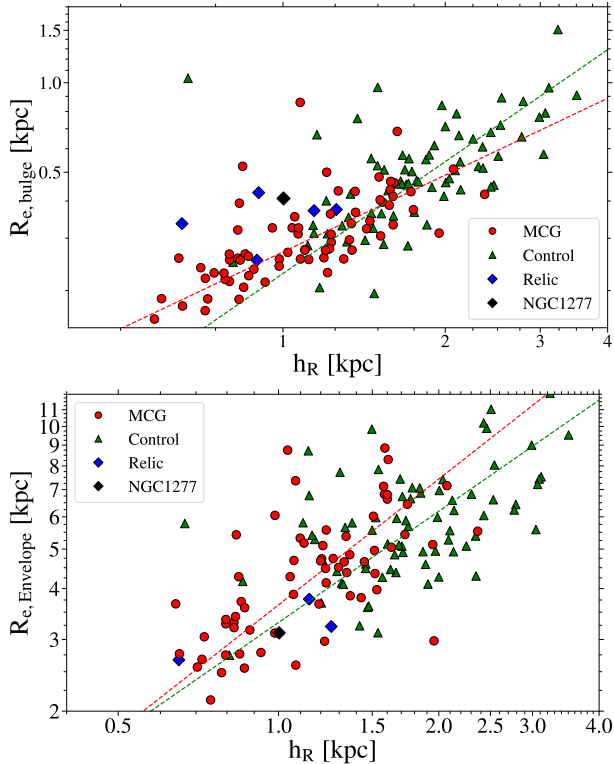


**Figure 6.** Coupling between structural components. Disk scale length versus bulge effective radius is shown in the top panel, and disk scale length versus envelope effective radius in the bottom panel. MCGs are shown as red circles, CSGs as green triangles, and relics as blue diamonds with the prototypical relic galaxy NGC 1277 highlighted as a black diamond. A linear fit to the combined MCG and relic distribution is indicated by the dashed red line, while the dashed green line shows the best fit to the CSG distribution. Galaxies best fitted with a four-component model are excluded from the bottom panel.

the fraction of accreted stars is below 10%. They then applied this classification to a sample of nearby compact elliptical galaxies (which includes all galaxies in our relic sample except for PGC12557) by comparing their observed dynamics to those of the simulated systems. Zhu et al. (2025) found that the relic galaxies Mrk 1216, NGC 1270, and NGC 1271—all of which in our analysis require four structural components—and NGC 1281, which has a relatively low envelope ellipticity ( $\epsilon_{\text{env}} = 0.2$ ), are likely to have experienced mergers that significantly altered their internal structure. The remaining relic galaxies were classified as “merger-free”.

We now turn to MCGs with high envelope ellipticity ( $\epsilon_{\text{env}} > 0.45$ ), comprising 29% of the sample. Two representative examples, MCGs ID 24 and 44, are shown in the bottom panels of Fig. 7. This group is morphologically homogeneous, with members resembling compact, thicker versions of the S0s in the control sample.

Given their high ellipticity, we interpret their envelopes as thick disks.

Simulations suggest that thick disks form through a combination of early in situ star formation and later growth via accretion and dynamical heating of thin disk stars (Park et al. 2021; Yu et al. 2021; Pinna et al. 2024; Yi et al. 2024), with the relative contributions varying between galaxies. While thin disks can survive minor mergers (Bournaud et al. 2007; Villalobos & Helmi 2008; Qu et al. 2011), mergers with stellar mass ratios of 0.1–0.2 often leave only 15–25% of the stellar mass in a surviving thin disk (Villalobos & Helmi 2008). This is at odds with the observed  $D/T \sim 0.4$  in MCGs, moreover only 4% of the sample have  $D/T < 0.25$ . Therefore, if high- $\epsilon_{\text{env}}$  envelopes formed via minor mergers, these events must have been gas-rich, allowing for substantial thin-disk regrowth. Alternatively, a predominantly in-situ formation of high-ellipticity envelopes is also plausible. We note that the relics classified as merger-free by Zhu et al. (2025) almost invariably have  $\epsilon_{\text{env}} \geq 0.5$ , supporting this scenario.

This discussion raises the broader question of the role mergers play in the formation of MCGs. Simulations suggest that this role is limited: in Lohmann et al. (2023), we analyzed simulated MCG analogs at  $z = 0$  in Illustris TNG100 and found a median ex situ stellar mass fraction of only  $\sim 7\%$ , although this can reach  $\sim 20\%$  in some cases. Similarly, Kurinchi-Vendhan et al. (2024) find that mergers play a minimal role in the quenching of star formation in quiescent galaxies at  $z > 3$ . In contrast, Pathak et al. (2021) report that the majority of young quiescent galaxies at  $z \sim 2$  experienced significant mergers, although this fraction is much smaller in older quiescent systems. An important caveat, however, is whether these simulated analogs adequately capture the formation physics of such rare, extreme galaxies.

An observational perspective is provided by morphological studies of  $z > 2$  starbursts and sub-millimeter galaxies, the likely progenitors of high-redshift compact quiescent galaxies. Studies with the Atacama Large Millimeter/submillimeter Array (ALMA) and the James Webb Space Telescope (JWST) consistently find that the majority of these galaxies show signs of interactions, with major merger fractions of  $\sim 20 - 25\%$  and minor merger fractions of  $\sim 40 - 50\%$  (Gómez-Guijarro et al. 2018; Colina et al. 2023; Gillman et al. 2024; Polletta et al. 2024; Ren et al. 2025; Hodge et al. 2025). However, galaxies with undisturbed morphologies make up 20–40% of the population, implying secular dynamical processes can also play a role in shaping their morphology (Ren et al. 2025; Hodge et al. 2025; Stacey et al. 2025).

Taken together, these results suggest that early gas-rich mergers are likely to play an important role in the formation of many MCGs, although a non-negligible fraction of merger-free MCGs is expected.

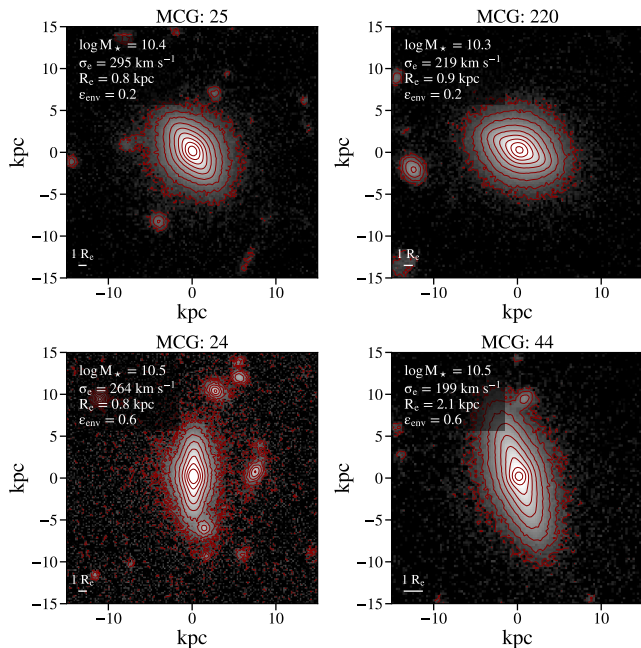


**Figure 7.** Top panels: example  $r$ -band images of MCGs with outer ellipticity  $\epsilon_{\text{env}} < 0.3$ . Bottom panels: example  $r$ -band images of MCGs with outer ellipticity  $\epsilon_{\text{env}} > 0.45$ . Overlaid are isophotal contours spanning surface brightness levels from  $\mu = 18.5$  to  $26 \text{ mag arcsec}^{-2}$ , highlighting the galaxies’ morphological structure.

### 5.3. Are MCGs Relics of the High Redshift Universe?

There is no consensus definition of relic galaxies, with different studies adopting varying criteria, but the following conditions are usually required to be satisfied (Trujillo et al. 2014; Ferré-Mateu et al. 2015, 2017; Tortora et al. 2025): I) the galaxy must host predominantly old ( $\gtrsim 10 \text{ Gyr}$ ) stellar populations out to a few  $R_e$ , with the fraction of younger stellar populations below  $\sim 10\%$ ; II) it should show a regular velocity field and exhibit an undisturbed morphology, as these are features consistent with a passive post-quenching evolution; III) the galaxy should be massive and compact. This last point is particularly ill-defined, as the mass and size thresholds vary significantly across studies. While a quantitative estimate of the fraction of MCGs satisfying the relic galaxy criteria can not be obtained with the currently available data, we believe a qualitative discussion on this topic is pertinent given the structural similarities between MCGs and relics highlighted earlier in this paper.

We begin by assessing criterion II). Based on a visual inspection of the HSC images, we identify only ten MCGs with minor asymmetries or disturbances that could plausibly be associated with either minor mergers or tidal stripping. It is important to bear in mind that such signatures typically remain visible for only a few Gyr (Mancillas et al. 2019), and therefore trace only re-

cent merger activity. However, it is unlikely that more than a small fraction of MCGs experienced significant dry merging at earlier times, given that their high  $D/T$  ratios are inconsistent with the expected for remnants of dry mergers with mass ratios  $> 0.1$ , as discussed in the previous section. We therefore expect that a significant fraction of MCGs satisfy criterion II).

To assess criteria I) and III), we present in Fig. 8 the size–mass distribution of MCGs and relic galaxies, color-coded by mass-weighted stellar population age. CSGs are also shown for comparison. The dashed, dot-dashed, and solid lines mark the compactness thresholds proposed by van der Wel et al. (2014), Barro et al. (2017), and Spiniello et al. (2021), respectively. Stellar ages for MCGs were taken from Clerici et al. (2024). Ages for CSGs and relic galaxies (except Mrk 1266) were derived from their SDSS spectra following the methodology of Clerici et al. (2024), while the age of Mrk 1266, which has no SDSS spectrum available, was taken from Ferré-Mateu et al. (2017). Within the region covered by the SDSS fiber ( $1.4 \pm 0.5 R_e$  on average in our sample), MCGs typically exhibit ages comparable to those of relics and older than those of CSGs, with only one galaxy younger than 10 Gyr. Given the arguments presented above against significant dry merging, and considering the envelope-origin scenarios discussed earlier, which suggest that the envelope was largely in place by  $z \gtrsim 2$ , it is plausible that MCGs generally host similarly old stellar populations out to several  $R_e$ , therefore we expect a significant fraction fulfills criterion I, although spatially resolved spectroscopy is required to confirm this. Regarding compactness (criterion III), 2 MCGs satisfy the Spiniello et al. (2021) threshold, 7 meet the van der Wel et al. (2014) threshold, and 23 fulfill the Barro et al. (2017) criterion. Since all three relic criteria (I–III) must be satisfied simultaneously, only a few MCGs in our sample qualify as relic galaxy candidates, despite the large fraction that show undisturbed morphologies and host very old stellar populations within the fiber aperture.

To explore this further, we also show in Fig. 8 the distribution in the size–mass plane of  $1.5 < z < 3$  quiescent galaxies extracted from the 3D-HST survey (Brammer et al. 2012; Skelton et al. 2014; Momcheva et al. 2016). Following Wuyts et al. (2007) and Williams et al. (2009), 3D-HST galaxies were classified as star-forming or quiescent based on their rest-frame colors. We extracted their sizes from van der Wel et al. (2014). Some 3D-HST quiescent galaxies occupy the same region as MCGs, and some are even larger, meaning that many high- $z$  quiescent galaxies, if they evolved passively, would not satisfy the relic criteria at  $z \sim 0$ . This reflects the fact that the compactness thresholds were designed to select local analogues with sizes at the lower end of the high- $z$  size distribution. Therefore, a passively evolving galaxy with a relatively large size may fulfill criteria I) and II) but fail to meet the compactness requirement (criterion

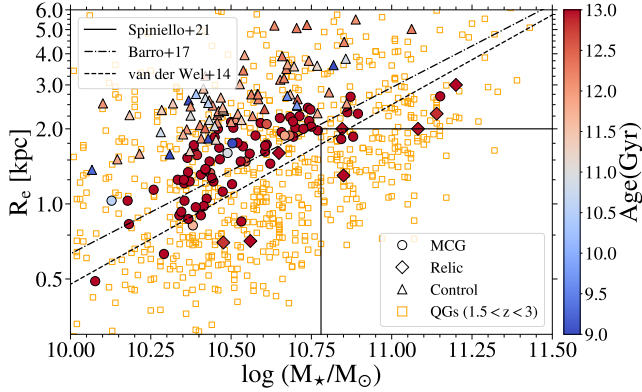


**Figure 8.** Distribution of MCGs, CSGs, relics, and  $1.5 < z < 3$  quiescent galaxies in the  $M_*$ – $R_e$  plane. MCGs, CSGs, and relics are color-coded by stellar population age. The dashed, dot-dashed, and solid lines represent the compactness thresholds proposed by van der Wel et al. (2014), Barro et al. (2017), and Spiniello et al. (2021), respectively. Despite their differing sizes, relics and MCGs exhibit similarly old stellar populations. In contrast, CSGs are significantly younger, even though some have sizes comparable to those of MCGs.

III), and thus would not be classified as a relic under current definitions. This limited overlap with compactness thresholds raises the question of how well local relic definitions capture the properties of the broader high-redshift quiescent population.

High-redshift quiescent galaxies differ from their local counterparts not only in the size–mass relation but also in the stellar mass–velocity dispersion ( $M_*$ – $\sigma_e$ ) relation. As illustrated in Fig. 1, the  $M_*$ – $\sigma_e$  relation has undergone significant evolution since  $z = 2$ . In Clerici et al. (2024), we demonstrated that the stellar population properties of quiescent galaxies systematically vary with their location in the  $M_*$ – $\sigma_e$  plane. Massive compact galaxies,  $+2\sigma$  outliers above the local  $M_*$ – $\sigma_e$  relation by definition, are older and more  $\alpha$ -enhanced than quiescent galaxies with similar  $\sigma_e$  along the central trend. These differences diminish with increasing  $\sigma_e$  and largely disappear at  $\sigma_e \gtrsim 225 \text{ km s}^{-1}$ , where galaxies on the local relation exhibit comparable ages and  $\alpha$ -enhancements. A similar trend was reported by Graves et al. (2009a) for elliptical galaxies. Furthermore, Graves et al. (2009b) found that, at fixed  $\sigma_e$ , stellar population properties of ellipticals show no dependence on  $R_e$  (and thus on compactness), a result we also confirm for MCGs. Consequently, quiescent galaxy samples selected solely on the basis of compactness—without considering the  $M_*$ – $\sigma_e$  relation—include systems spanning a wide range of stellar ages, from ancient galaxies to young post-starburst objects (Ferré-Mateu et al. 2012; Damjanov et al. 2013; Zahid et al. 2016; Schnorr-Müller et al. 2021; Spiniello et al. 2021). An age diversity is also visible in Fig. 8, where CSGs

consistently exhibit younger ages than MCGs regardless of their size, although to a smaller degree than in the aforementioned studies.

The results presented in Sec. 4.3 hint at a possible additional drawback of strict compactness thresholds: they tend to select galaxies with more massive bulges, thereby preferentially excluding disk-dominated systems. However, our strict selection based on the  $M_*$ – $\sigma_e$  relation is also subject to biases. Among the 225 HSC-observed MCGs presented in Paper I, 75 were classified as edge-on systems, representing a disproportionate number of highly inclined galaxies. This reflects a selection bias introduced by the contribution of rotational motion to the integrated velocity dispersion, which leads to systematically higher  $\sigma_e$  measurements in highly inclined systems. A similar inclination bias is evident in the Yıldırım et al. (2017) compact elliptical galaxy sample, where high velocity dispersion was a selection criterion: all 17 galaxies have inclinations  $\gtrsim 70^\circ$ . A possible way to mitigate these biases may be to combine constraints from both the  $M_*$ – $R_e$  and  $M_*$ – $\sigma_e$  relations, using thresholds less stringent than those adopted here and in previous studies. We leave the exploration of such combined selection strategies for future work.

#### 5.4. Structural Similarities between MCGs and High- $z$ Quiescent Galaxies

In this study, we have shown that the morphological structure of MCGs is well described by a combination of compact bulges and disks embedded within a stellar envelope of varying intrinsic ellipticity, with the disk generally being the dominant component. Given that the stellar population properties of MCGs indicate a formation epoch at  $z \gtrsim 2$ , one would expect a significant fraction of high- $z$  quiescent galaxies to exhibit similar structures if MCGs indeed underwent passive evolution. Observations provide suggestive evidence supporting this expectation.

Davari et al. (2017) performed bulge–disk decompositions of massive ( $\log(M_*/M_\odot) > 10.7$ ) quiescent galaxies at  $0.5 < z < 2.5$  in the CANDELS fields, finding that at  $z \sim 2$ , more than 50% of galaxies have  $B/T \leq 0.5$ . Furthermore, spatially resolved stellar kinematics of massive quiescent galaxies at  $z = 1–3$  reveals the majority are fast rotators, consistent with the presence of stellar disks. However, the measured values of the spin parameter  $\lambda_e$  show considerable variation, suggesting differences in the degree of rotational support among galaxies (D’Eugenio et al. 2024; Pascalau et al. 2025; Forrest et al. 2025; Slob et al. 2025).

A few  $z \gtrsim 2$  quiescent galaxies have been the subject of detailed studies, allowing for a deeper comparison. A double Sérsic decomposition of galaxies MRG-2129 and MRG-M0138 by Newman et al. (2018) reveals edge-on disks embedded in mildly flattened envelopes ( $\epsilon \approx 0.2$  and  $\epsilon \approx 0.3$ , respectively) with  $n \sim 1$  and no evidence of  $n = 4$  classical bulges, sharing notable similarities

with MCGs. Similarly, a bulge+disk decomposition of the  $z \sim 3$  quiescent galaxy ZF-UDS-7329 by [Turner et al. \(2025\)](#) shows an edge-on disk and an  $n \sim 2$  bulge, further reinforcing the disky nature of high- $z$  quiescent galaxies. Taken together, these results suggest that the structural properties of MCGs are consistent with those of massive quiescent galaxies at  $z \sim 2-3$ , supporting an evolutionary link between the two populations.

## 6. SUMMARY AND CONCLUSIONS

In this work, we presented the results of a multi-component morphological decomposition of  $r$ -band HSC images for a sample of 75 edge-on massive compact galaxies, alongside an equal-sized control sample of edge-on S0 galaxies matched in stellar mass and redshift, as well as a sample of 8 relic galaxies with HST imaging. Galaxies were modeled with three structural components: a Sérsic bulge, an edge-on disk, and an exponential stellar envelope.

We find that:

- The smaller sizes of MCGs compared to CSGs are not driven preferentially by a single component. Instead, all structural components are more compact. MCGs exhibit more compact bulges (median  $R_{e,\text{bulge}} \sim 0.3$  kpc vs. 0.5 kpc) and envelopes ( $R_{e,\text{env}} \sim 4.4$  kpc vs. 5.7 kpc), as well as shorter disks ( $h_R \sim 1.1$  kpc vs. 1.7 kpc);
- MCGs host thicker disks ( $h_R/z_0 \sim 3.9$  vs. 5.3) and rounder envelopes (median  $\epsilon_{\text{env}} \sim 0.40$  vs. 0.56) than CSGs;
- The flux fractions of the structural components are broadly consistent between the two samples, with median  $B/T \sim 0.3$  and  $D/T \sim 0.4$  in both;
- Considering the  $z_0$  distributions of MCGs and CSGs largely overlap while MCG disks are systematically shorter at fixed stellar mass, we argue that MCG disks likely have higher stellar velocity dispersions. We suggest this difference could, at least in part, be due to the star-forming progenitors of MCGs hosting more turbulent gas disks;
- We find that the sizes of the structural components are coupled in MCGs, suggesting that the formation and growth of the disk, bulge, and envelope are linked. This coupling, together with the survival of a disk component with  $D/T \sim 0.4$ , argues against dry minor mergers as the dominant mechanism responsible for building the envelope, at least for the MCG population as a whole: repeated minor mergers would heat and disrupt the thin disk, and deposit material preferentially at large radii without producing the observed coupling between component sizes;

- A comparison with 8 relic galaxies reveals that MCGs and relics share many structural properties, although MCGs are typically somewhat larger. Relics also exhibit compact bulges and disks embedded within stellar envelopes. The structural components of MCGs and relics are consistent with following the same size–mass relations, distinct from those followed by the components of CSGs. This supports the idea that relics and MCGs belong to the same structural family;
- Despite these similarities, relics tend to have higher  $B/T$  ratios (median 0.37 vs. 0.26). This is likely to be, at least in part, a contributing factor to the smaller sizes of relics compared to MCGs. At fixed total stellar mass, higher  $B/T$  ratios are associated with smaller galaxy sizes not only because of the larger bulge contribution, but also because the disk and envelope carry less of the total mass — and since component sizes scale with component mass, this makes all components smaller simultaneously;
- Given that higher  $B/T$  ratios lead to smaller galaxy sizes, the strict compactness criteria frequently employed in relic searches are likely to bias the selected samples toward bulge-dominated galaxies;
- The envelope ellipticities of MCGs and relics span a wide range,  $\epsilon_{\text{Env}} \sim 0-0.7$ . This suggests that envelopes correspond to different physical structures in different galaxies. Based on comparisons with simulations and  $z > 2$  starburst observations, we propose that low-ellipticity envelopes ( $\epsilon_{\text{Env}} \lesssim 0.2$ ) are stellar haloes formed in gas-rich major mergers at  $z \gtrsim 2$ , while the most flattened ones ( $\epsilon_{\text{Env}} \gtrsim 0.5$ ) are thick disks, formed either in-situ or through gas-rich minor mergers. The nature of envelopes with intermediate ellipticities remains ambiguous from photometry alone;
- The majority of MCGs show undisturbed morphologies, and within the region probed by SDSS spectra ( $1.4 \pm 0.5 R_e$  on average) they exhibit old stellar populations ( $\gtrsim 10$  Gyr), characteristics comparable to those of confirmed relics. However, most MCGs fail to meet the compactness thresholds commonly adopted in relic searches: only 2 satisfy the [Spiniello et al. \(2021\)](#) criterion, 7 meet the [van der Wel et al. \(2014\)](#) threshold, and 23 fulfill the [Barro et al. \(2017\)](#) criterion. Since spatially resolved spectroscopy is required to confirm that old stellar populations extend to several  $R_e$ , a definitive assessment on the fraction of passively evolving MCGs is not yet possible. Nonetheless, the structural, morphological, and stellar population similarities between MCGs and relics suggest

that a significant fraction of MCGs are members of a population of passively evolved compact galaxies that current relic search criteria fail to capture.

#### ACKNOWLEDGMENTS

ASM acknowledges the financial support from the Brazilian National Council for Scientific and Technological Development (CNPq) and from the Fundação de Amparo à Pesquisa do Estado do Rio Grande do

Sul (FAPERGS). KSC acknowledges the Coordination for the Improvement of Higher Education Personnel (CAPES) for the financial support (88887.629089/2021-00). FP acknowledges support from the Horizon Europe research and innovation programme under the Maria Skłodowska-Curie grant “TraNSLate” No 101108180. ACSM acknowledges support from the European Southern Observatory (ESO) as an SCV visitor at the ESO Science Office in Vitacura, as well as financial support from CAPES (process no. 88887.001289/2024-00). MT thanks the support from CNPq (process 307111/2025-3) and from FAPERGS.

#### REFERENCES

- Abolfathi, B., Aguado, D. S., Aguilar, G., et al. 2018, *ApJS*, 235, 42, doi: [10.3847/1538-4365/aa9e8a](https://doi.org/10.3847/1538-4365/aa9e8a)
- Aguerri, J. A. L., Elias-Rosa, N., Corsini, E. M., & Muñoz-Tuñón, C. 2005, *A&A*, 434, 109, doi: [10.1051/0004-6361:20041743](https://doi.org/10.1051/0004-6361:20041743)
- Aihara, H., Armstrong, R., Bickerton, S., et al. 2018, *PASJ*, 70, S8, doi: [10.1093/pasj/psx081](https://doi.org/10.1093/pasj/psx081)
- Anderson, J. 2016, *Empirical Models for the WFC3/IR PSF*, Instrument Science Report WFC3 2016-12, 42 pages
- Anderson, J., & King, I. R. 2000, *PASP*, 112, 1360, doi: [10.1086/316632](https://doi.org/10.1086/316632)
- Barro, G., Faber, S. M., Pérez-González, P. G., et al. 2013, *ApJ*, 765, 104, doi: [10.1088/0004-637X/765/2/104](https://doi.org/10.1088/0004-637X/765/2/104)
- Barro, G., Faber, S. M., Koo, D. C., et al. 2017, *ApJ*, 840, 47, doi: [10.3847/1538-4357/aa6b05](https://doi.org/10.3847/1538-4357/aa6b05)
- Bertin, E., & Arnouts, S. 1996, *A&AS*, 117, 393, doi: [10.1051/aas:1996164](https://doi.org/10.1051/aas:1996164)
- Binney, J., & Tremaine, S. 2008, *Galactic Dynamics: Second Edition*
- Birkin, J. E., Puglisi, A., Swinbank, A. M., et al. 2024, *MNRAS*, 531, 61, doi: [10.1093/mnras/stae1089](https://doi.org/10.1093/mnras/stae1089)
- Bosch, J., Armstrong, R., Bickerton, S., et al. 2018, *PASJ*, 70, S5, doi: [10.1093/pasj/psx080](https://doi.org/10.1093/pasj/psx080)
- Bournaud, F., Jog, C. J., & Combes, F. 2007, *A&A*, 476, 1179, doi: [10.1051/0004-6361:20078010](https://doi.org/10.1051/0004-6361:20078010)
- Brammer, G. B., van Dokkum, P. G., Franx, M., et al. 2012, *ApJS*, 200, 13, doi: [10.1088/0067-0049/200/2/13](https://doi.org/10.1088/0067-0049/200/2/13)
- Brinchmann, J., Charlot, S., White, S. D. M., et al. 2004, *MNRAS*, 351, 1151, doi: [10.1111/j.1365-2966.2004.07881.x](https://doi.org/10.1111/j.1365-2966.2004.07881.x)
- Buitrago, F., Ferreras, I., Kelvin, L. S., et al. 2018, *A&A*, 619, A137, doi: [10.1051/0004-6361/201833785](https://doi.org/10.1051/0004-6361/201833785)
- Bundy, K., Scarlata, C., Carollo, C. M., et al. 2010, *ApJ*, 719, 1969, doi: [10.1088/0004-637X/719/2/1969](https://doi.org/10.1088/0004-637X/719/2/1969)
- Cannarozzo, C., Sonnenfeld, A., & Nipoti, C. 2020, *MNRAS*, 498, 1101, doi: [10.1093/mnras/staa2147](https://doi.org/10.1093/mnras/staa2147)
- Cappellari, M., Bacon, R., Bureau, M., et al. 2006, *MNRAS*, 366, 1126, doi: [10.1111/j.1365-2966.2005.09981.x](https://doi.org/10.1111/j.1365-2966.2005.09981.x)
- Carollo, C. M., Scarlata, C., Stiavelli, M., Wyse, R. F. G., & Mayer, L. 2007, *ApJ*, 658, 960, doi: [10.1086/511125](https://doi.org/10.1086/511125)
- Carollo, C. M., Bschorr, T. J., Renzini, A., et al. 2013, *ApJ*, 773, 112, doi: [10.1088/0004-637X/773/2/112](https://doi.org/10.1088/0004-637X/773/2/112)
- Clerici, K. S., Schnorr-Müller, A., Trevisan, M., & Ricci, T. V. 2024, *MNRAS*, 531, 1034, doi: [10.1093/mnras/stae1213](https://doi.org/10.1093/mnras/stae1213)
- Colina, L., Crespo Gómez, A., Álvarez-Márquez, J., et al. 2023, *A&A*, 673, L6, doi: [10.1051/0004-6361/202346535](https://doi.org/10.1051/0004-6361/202346535)
- Cook, R. H. W., Davies, L. J. M., Bellstedt, S., et al. 2025, *MNRAS*, 539, 2829, doi: [10.1093/mnras/staf575](https://doi.org/10.1093/mnras/staf575)
- Damjanov, I., Chilingarian, I., Hwang, H. S., & Geller, M. J. 2013, *ApJL*, 775, L48, doi: [10.1088/2041-8205/775/2/L48](https://doi.org/10.1088/2041-8205/775/2/L48)
- Damjanov, I., Zahid, H. J., Geller, M. J., et al. 2019, *ApJ*, 872, 91, doi: [10.3847/1538-4357/aaf97d](https://doi.org/10.3847/1538-4357/aaf97d)
- Davari, R. H., Ho, L. C., Mobasher, B., & Canalizo, G. 2017, *ApJ*, 836, 75, doi: [10.3847/1538-4357/836/1/75](https://doi.org/10.3847/1538-4357/836/1/75)
- Davidzon, I., Ilbert, O., Laigle, C., et al. 2017, *A&A*, 605, A70, doi: [10.1051/0004-6361/201730419](https://doi.org/10.1051/0004-6361/201730419)
- D’Eugenio, F., Pérez-González, P. G., Maiolino, R., et al. 2024, *Nature Astronomy*, 8, 1443, doi: [10.1038/s41550-024-02345-1](https://doi.org/10.1038/s41550-024-02345-1)
- Domínguez Sánchez, H., Huertas-Company, M., Bernardi, M., Tuccillo, D., & Fischer, J. L. 2018, *MNRAS*, 476, 3661, doi: [10.1093/mnras/sty338](https://doi.org/10.1093/mnras/sty338)
- Du, M., Ho, L. C., Debattista, V. P., et al. 2021, *ApJ*, 919, 135, doi: [10.3847/1538-4357/ac0e98](https://doi.org/10.3847/1538-4357/ac0e98)
- Erwin, P. 2015, *ApJ*, 799, 226, doi: [10.1088/0004-637X/799/2/226](https://doi.org/10.1088/0004-637X/799/2/226)
- Fagioli, M., Carollo, C. M., Renzini, A., et al. 2016, *ApJ*, 831, 173, doi: [10.3847/0004-637X/831/2/173](https://doi.org/10.3847/0004-637X/831/2/173)

- Ferré-Mateu, A., Mezcua, M., Trujillo, I., Balcels, M., & van den Bosch, R. C. E. 2015, *ApJ*, 808, 79, doi: [10.1088/0004-637X/808/1/79](https://doi.org/10.1088/0004-637X/808/1/79)
- Ferré-Mateu, A., Trujillo, I., Martín-Navarro, I., et al. 2017, *MNRAS*, 467, 1929, doi: [10.1093/mnras/stx171](https://doi.org/10.1093/mnras/stx171)
- Ferré-Mateu, A., Vazdekis, A., Trujillo, I., et al. 2012, *MNRAS*, 423, 632, doi: [10.1111/j.1365-2966.2012.20897.x](https://doi.org/10.1111/j.1365-2966.2012.20897.x)
- Forrest, B., Muzzin, A., Marchesini, D., et al. 2025, arXiv e-prints, arXiv:2508.10987, doi: [10.48550/arXiv.2508.10987](https://doi.org/10.48550/arXiv.2508.10987)
- Gadotti, D. A. 2026, *MNRAS*, 545, staf2072, doi: [10.1093/mnras/staf2072](https://doi.org/10.1093/mnras/staf2072)
- Gillman, S., Smail, I., Gullberg, B., et al. 2024, *A&A*, 691, A299, doi: [10.1051/0004-6361/202451006](https://doi.org/10.1051/0004-6361/202451006)
- Gómez-Guijarro, C., Toft, S., Karim, A., et al. 2018, *ApJ*, 856, 121, doi: [10.3847/1538-4357/aab206](https://doi.org/10.3847/1538-4357/aab206)
- Graves, G. J., Faber, S. M., & Schiavon, R. P. 2009a, *ApJ*, 693, 486, doi: [10.1088/0004-637X/693/1/486](https://doi.org/10.1088/0004-637X/693/1/486)
- . 2009b, *ApJ*, 698, 1590, doi: [10.1088/0004-637X/698/2/1590](https://doi.org/10.1088/0004-637X/698/2/1590)
- He, W.-T., Du, M., Li, Z.-Y., & Li, Y. 2025, *A&A*, 699, A99, doi: [10.1051/0004-6361/202554551](https://doi.org/10.1051/0004-6361/202554551)
- Ho, D. E., Imai, K., King, G., & Stuart, E. A. 2011, *Journal of Statistical Software*, 42, 1, <http://www.jstatsoft.org/v42/i08/>
- Hodge, J. A., da Cunha, E., Kendrew, S., et al. 2025, *ApJ*, 978, 165, doi: [10.3847/1538-4357/ad9a52](https://doi.org/10.3847/1538-4357/ad9a52)
- Jiang, F., van Dokkum, P., Bezanson, R., & Franx, M. 2012, *ApJL*, 749, L10, doi: [10.1088/2041-8205/749/1/L10](https://doi.org/10.1088/2041-8205/749/1/L10)
- Kurinchi-Vendhan, S., Farcy, M., Hirschmann, M., & Valentino, F. 2024, *MNRAS*, 534, 3974, doi: [10.1093/mnras/stae2297](https://doi.org/10.1093/mnras/stae2297)
- Lange, R., Moffett, A. J., Driver, S. P., et al. 2016, *MNRAS*, 462, 1470, doi: [10.1093/mnras/stw1495](https://doi.org/10.1093/mnras/stw1495)
- Lasker, R., van den Bosch, R. C. E., van de Ven, G., et al. 2013, *MNRAS*, 434, L31, doi: [10.1093/mnrasl/slt070](https://doi.org/10.1093/mnrasl/slt070)
- Laurikainen, E., Salo, H., Buta, R., & Knapen, J. H. 2009, *ApJL*, 692, L34, doi: [10.1088/0004-637X/692/1/L34](https://doi.org/10.1088/0004-637X/692/1/L34)
- Laurikainen, E., Salo, H., Buta, R., Knapen, J. H., & Comerón, S. 2010, *MNRAS*, 405, 1089, doi: [10.1111/j.1365-2966.2010.16521.x](https://doi.org/10.1111/j.1365-2966.2010.16521.x)
- Lim, S. H., Mo, H. J., Lu, Y., Wang, H., & Yang, X. 2017, *MNRAS*, 470, 2982, doi: [10.1093/mnras/stx1462](https://doi.org/10.1093/mnras/stx1462)
- Lohmann, F. S., Schnorr-Müller, A., Trevisan, M., Ricci, T. V., & Clerici, K. S. 2023, *MNRAS*, 524, 5266, doi: [10.1093/mnras/stad2176](https://doi.org/10.1093/mnras/stad2176)
- Mancillas, B., Duc, P.-A., Combes, F., et al. 2019, *A&A*, 632, A122, doi: [10.1051/0004-6361/201936320](https://doi.org/10.1051/0004-6361/201936320)
- Momcheva, I. G., Brammer, G. B., van Dokkum, P. G., et al. 2016, *ApJS*, 225, 27, doi: [10.3847/0067-0049/225/2/27](https://doi.org/10.3847/0067-0049/225/2/27)
- Naab, T., & Ostriker, J. P. 2009, *ApJ*, 690, 1452, doi: [10.1088/0004-637X/690/2/1452](https://doi.org/10.1088/0004-637X/690/2/1452)
- Nedkova, K. V., Häußler, B., Marchesini, D., et al. 2024, *MNRAS*, 532, 3747, doi: [10.1093/mnras/stae1702](https://doi.org/10.1093/mnras/stae1702)
- Newman, A. B., Belli, S., Ellis, R. S., & Patel, S. G. 2018, *ApJ*, 862, 125, doi: [10.3847/1538-4357/aacd4d](https://doi.org/10.3847/1538-4357/aacd4d)
- Noordermeer, E., & van der Hulst, J. M. 2007, *MNRAS*, 376, 1480, doi: [10.1111/j.1365-2966.2007.11532.x](https://doi.org/10.1111/j.1365-2966.2007.11532.x)
- Oser, L., Ostriker, J. P., Naab, T., Johansson, P. H., & Burkert, A. 2010, *ApJ*, 725, 2312, doi: [10.1088/0004-637X/725/2/2312](https://doi.org/10.1088/0004-637X/725/2/2312)
- Park, M. J., Yi, S. K., Peirani, S., et al. 2021, *ApJS*, 254, 2, doi: [10.3847/1538-4365/abe937](https://doi.org/10.3847/1538-4365/abe937)
- Pascalau, R. G., D'Eugenio, F., Tacchella, S., et al. 2025, arXiv e-prints, arXiv:2505.06349, doi: [10.48550/arXiv.2505.06349](https://doi.org/10.48550/arXiv.2505.06349)
- Pathak, D., Belli, S., & Weinberger, R. 2021, *ApJL*, 916, L23, doi: [10.3847/2041-8213/ac13a7](https://doi.org/10.3847/2041-8213/ac13a7)
- Pinna, F., Walo-Martín, D., Grand, R. J. J., et al. 2024, *A&A*, 683, A236, doi: [10.1051/0004-6361/202347388](https://doi.org/10.1051/0004-6361/202347388)
- Polletta, M., Frye, B. L., Garuda, N., et al. 2024, *A&A*, 690, A285, doi: [10.1051/0004-6361/202450671](https://doi.org/10.1051/0004-6361/202450671)
- Qu, Y., Di Matteo, P., Lehnert, M. D., & van Driel, W. 2011, *A&A*, 530, A10, doi: [10.1051/0004-6361/201015224](https://doi.org/10.1051/0004-6361/201015224)
- Querejeta, M., Eliche-Moral, M. C., Tapia, T., et al. 2015, *A&A*, 573, A78, doi: [10.1051/0004-6361/201424303](https://doi.org/10.1051/0004-6361/201424303)
- Ren, J., Liu, F. S., Li, N., et al. 2025, *ApJ*, 982, 200, doi: [10.3847/1538-4357/adb961](https://doi.org/10.3847/1538-4357/adb961)
- Rosenbaum, P. R., & Rubin, D. B. 1983, *Biometrika*, 70, 41, doi: [10.1093/biomet/70.1.41](https://doi.org/10.1093/biomet/70.1.41)
- Salim, S., Boquien, M., & Lee, J. C. 2018, *ApJ*, 859, 11, doi: [10.3847/1538-4357/aabf3c](https://doi.org/10.3847/1538-4357/aabf3c)
- Schnorr-Müller, A., Trevisan, M., Riffel, R., et al. 2021, *MNRAS*, 507, 300, doi: [10.1093/mnras/stab2116](https://doi.org/10.1093/mnras/stab2116)
- Simard, L., Mendel, J. T., Patton, D. R., Ellison, S. L., & McConnachie, A. W. 2011, *ApJS*, 196, 11, doi: [10.1088/0067-0049/196/1/11](https://doi.org/10.1088/0067-0049/196/1/11)
- Skelton, R. E., Whitaker, K. E., Momcheva, I. G., et al. 2014, *ApJS*, 214, 24, doi: [10.1088/0067-0049/214/2/24](https://doi.org/10.1088/0067-0049/214/2/24)
- Slob, M., Kriek, M., de Graaff, A., et al. 2025, *A&A*, 702, A110, doi: [10.1051/0004-6361/202555812](https://doi.org/10.1051/0004-6361/202555812)
- Slodkowski Clerici, K., Schnorr-Müller, A., Santiago-Menezes, A. C., et al. 2026, arXiv e-prints, arXiv:2605.09733, <https://arxiv.org/abs/2605.09733>
- Spiniello, C., Tortora, C., D'Ago, G., et al. 2021, *A&A*, 646, A28, doi: [10.1051/0004-6361/202038936](https://doi.org/10.1051/0004-6361/202038936)
- Spitzer, Jr., L. 1942, *ApJ*, 95, 329, doi: [10.1086/144407](https://doi.org/10.1086/144407)

- Stacey, H. R., Kaasinen, M., O’Riordan, C. M., et al. 2025, *A&A*, 693, L17, doi: [10.1051/0004-6361/202452518](https://doi.org/10.1051/0004-6361/202452518)
- Tortora, C., Tozzi, G., Agapito, G., et al. 2025, *MNRAS*, 540, 2555, doi: [10.1093/mnras/staf831](https://doi.org/10.1093/mnras/staf831)
- Trujillo, I., Ferré-Mateu, A., Balcells, M., Vazdekis, A., & Sánchez-Blázquez, P. 2014, *ApJL*, 780, L20, doi: [10.1088/2041-8205/780/2/L20](https://doi.org/10.1088/2041-8205/780/2/L20)
- Tsukui, T., Wisnioski, E., Bland-Hawthorn, J., & Freeman, K. 2025, *MNRAS*, 540, 3493, doi: [10.1093/mnras/staf604](https://doi.org/10.1093/mnras/staf604)
- Turner, C., Tacchella, S., D’Eugenio, F., et al. 2025, *MNRAS*, 537, 1826, doi: [10.1093/mnras/staf128](https://doi.org/10.1093/mnras/staf128)
- van der Kruit, P. C., & Searle, L. 1981, *A&A*, 95, 105
- van der Wel, A., Franx, M., van Dokkum, P. G., et al. 2014, *ApJ*, 788, 28, doi: [10.1088/0004-637X/788/1/28](https://doi.org/10.1088/0004-637X/788/1/28)
- Villalobos, Á., & Helmi, A. 2008, *MNRAS*, 391, 1806, doi: [10.1111/j.1365-2966.2008.13979.x](https://doi.org/10.1111/j.1365-2966.2008.13979.x)
- Williams, C. C., Giavalisco, M., Bezanson, R., et al. 2017, *ApJ*, 838, 94, doi: [10.3847/1538-4357/aa662f](https://doi.org/10.3847/1538-4357/aa662f)
- Williams, R. J., Quadri, R. F., Franx, M., van Dokkum, P., & Labbé, I. 2009, *ApJ*, 691, 1879, doi: [10.1088/0004-637X/691/2/1879](https://doi.org/10.1088/0004-637X/691/2/1879)
- Wuyts, S., Labbé, I., Franx, M., et al. 2007, *ApJ*, 655, 51, doi: [10.1086/509708](https://doi.org/10.1086/509708)
- Yi, S. K., Jang, J. K., Devriendt, J., et al. 2024, *ApJS*, 271, 1, doi: [10.3847/1538-4365/ad0e71](https://doi.org/10.3847/1538-4365/ad0e71)
- Yıldırım, A., van den Bosch, R. C. E., van de Ven, G., et al. 2015, *MNRAS*, 452, 1792, doi: [10.1093/mnras/stv1381](https://doi.org/10.1093/mnras/stv1381)
- . 2017, *MNRAS*, 468, 4216, doi: [10.1093/mnras/stx732](https://doi.org/10.1093/mnras/stx732)
- Yu, S., Bullock, J. S., Klein, C., et al. 2021, *MNRAS*, 505, 889, doi: [10.1093/mnras/stab1339](https://doi.org/10.1093/mnras/stab1339)
- Zahid, H. J., Baeza Hochmuth, N., Geller, M. J., et al. 2016, *ApJ*, 831, 146, doi: [10.3847/0004-637X/831/2/146](https://doi.org/10.3847/0004-637X/831/2/146)
- Zhu, L., Chies-Santos, A. L., Moura, M. T., & Shi, H. 2025, *A&A*, 698, A195, doi: [10.1051/0004-6361/202453083](https://doi.org/10.1051/0004-6361/202453083)

**Table 3.** Summary of HST observations of MCGs. The table lists the MCG identifier, right ascension, declination, the associated HST proposal ID, the Principal Investigator (PI) of the program, and the instrument/filter combination used for the observations.

| MCG ID | RA (deg) | Dec (deg) | Proposal ID | PI          | Instrument / Filter |
|--------|----------|-----------|-------------|-------------|---------------------|
| 101    | 194.9083 | 27.8404   | 10861       | D. Carter   | ACS / F814W         |
| 108    | 144.0975 | 59.4158   | 12903       | L. C. Ho    | WFC3 / F105W        |
| 109    | 168.2287 | 13.4059   | 8719        | A. Edge     | WFPC2 / F606W       |
| 110    | 202.6897 | -1.8116   | 11202       | L. Koopmans | WFPC2 / F606W       |

**Table 4.** Structural properties of MCGs with available HST imaging. Reported values include stellar mass ( $M_*$ ), effective velocity dispersion ( $\sigma_e$ ), global effective radius ( $R_e$ ), bulge ellipticity ( $\epsilon_{\text{bulge}}$ ), Sérsic index of the bulge ( $n_{\text{bulge}}$ ), bulge effective radius ( $R_{e,\text{bulge}}$ ), bulge-to-total light ratio (B/T), disk scale length ( $h_R$ ), disk scale height ( $z_0$ ), disk flattening ( $h_R/z_0$ ), disk-to-total light ratio (D/T), envelope ellipticity ( $\epsilon_{\text{env}}$ ), envelope effective radius ( $R_{e,\text{env}}$ ), and envelope-to-total light ratio (Env/T). All radii are given in kpc.

| ID  | $\log(M_*/M_\odot)$ | $\sigma_e$             | $R_e$ | $\epsilon_{\text{bulge}}$ | $n_{\text{bulge}}$ | $R_{e,\text{bulge}}$ | B/T  | $h_R$ | $z_0$ | $h_R/z_0$ | D/T  | $\epsilon_{\text{env}}$ | $R_{e,\text{env}}$ | Env/T |
|-----|---------------------|------------------------|-------|---------------------------|--------------------|----------------------|------|-------|-------|-----------|------|-------------------------|--------------------|-------|
|     |                     | [ $\text{km s}^{-1}$ ] | [kpc] |                           |                    |                      |      |       |       |           |      |                         |                    |       |
| 101 | 10.5                | 227                    | 1.9   | 0.3                       | 1.9                | 0.26                 | 0.26 | 0.7   | 0.21  | 3.2       | 0.20 | 0.6                     | 2.8                | 0.54  |
| 108 | 10.5                | 207                    | 1.5   | 0.2                       | 2.0                | 0.16                 | 0.31 | 1.1   | 0.30  | 3.6       | 0.43 | 0.5                     | 2.5                | 0.26  |
| 109 | 10.5                | 249                    | 1.2   | –                         | –                  | < 0.2                | 0.22 | 0.7   | 0.12  | 5.8       | 0.43 | 0.4                     | 1.9                | 0.35  |
| 110 | 10.5                | 184                    | 2.0   | 0.5                       | 2.1                | 0.34                 | 0.37 | 1.0   | 0.24  | 4.0       | 0.21 | 0.6                     | 3.0                | 0.42  |

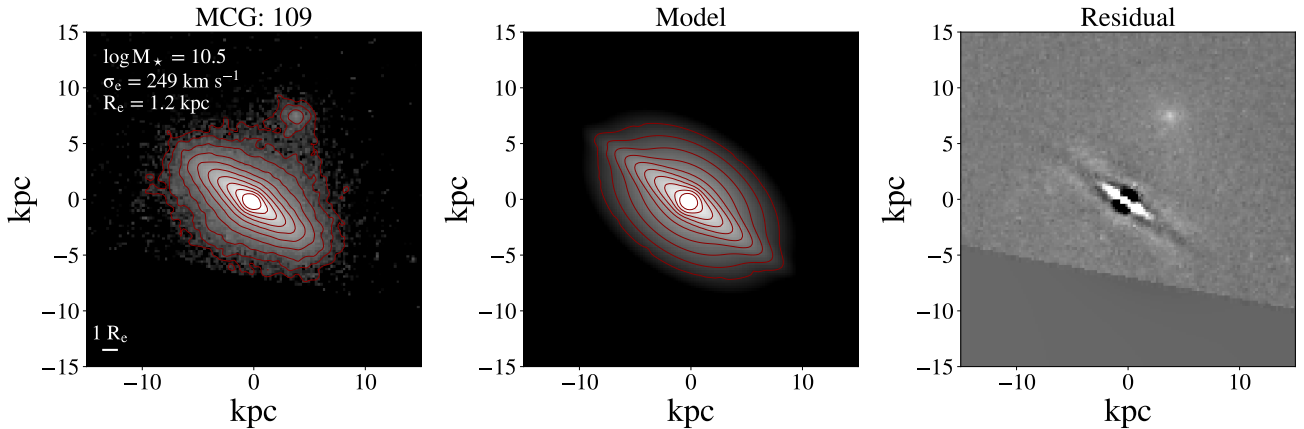


**Figure 9.** HST WFPC2/F606W image, best-fitting model, and residuals for MCG ID: 109. The bulge of this galaxy was fitted with a point source, which gives an upper limit of  $\sim 0.2$  kpc for  $R_{e,\text{bulge}}$ .

## APPENDIX

### A. MCGS WITH HST IMAGING

Of the 1858 SDSS MCGs in the Clerici et al. (2024) sample, four have HST archival imaging available. In table 3 we list the Proposal ID, PI, instrument and filter of these observations. We performed multi-component decomposition of these galaxies following the same strategy used for the HSC images. PSFs were built for each observation following the same strategy outlined in Sec. 3. The bulge of MCG ID: 109 was best fitted by a point source, so an upper limit for  $R_{e,\text{bulge}}$  is given in table 4. In Fig. 9 we show as an example the HST image, best fitting model and residuals for MCG ID 109.